The GPCR Smoothened on Cholinergic Interneurons Modulates Dopamine-associated Acetylcholine Dynamics

Uribe-Cano, S.[1,2] & Kottmann, A. H.[1,2,3]

[1]Department of Molecular, Cellular and Biomedical Sciences, CUNY School of Medicine at City College of New York, City University of New York, New York, NY, USA

[2]City University of New York Graduate Center, Neuroscience Collaborative, New York, NY, USA

[3]City University of New York Graduate Center, Molecular, Cellular and Developmental Subprogram, New York, NY, USA

Correspondence to: Dr. Andreas H. Kottmann, Dept. of Molecular, Cellular and Biomedical Research CUNY School of Medicine at City College of New York Center for Discovery and Innovation 85 St. Nicholas Terrace; 3-314, New York City, NY 10031; E-mail: AKottmann@med.cuny.edu

Abstract

The striatum is a hub for associative learning where fluctuations in dopamine (DA) and acetylcholine (ACh) dynamically regulate behavior. ACh is released by cholinergic interneurons (CIN), which integrate diverse inputs to contextualize DA signals and shape adaptive responses. Among these inputs, we previously observed that the GPCR Smoothened (Smo) on CIN suppresses L-DOPA-induced dyskinesias, a motor side-effect resulting from artificially elevated DA levels in the Parkinsonian brain. Here, we examine whether Smo signaling modulates ACh dynamics, its coordination with DA, and motor learning in the healthy brain. We find that CIN-specific Smo activity bidirectionally modulates ACh inhibition in response to both optogenetically evoked and endogenous DA. Smo relieves DA-associated ACh inhibition and permits its progressive modification with repeated DA release. These effects alter the temporal organization of ACh in the dorsolateral striatum and its coupling to DA, without affecting DA release itself. Behaviorally, Smo ablation from cholinergic neurons promotes initial motor learning at the expense of future behavioral flexibility. Together, these findings identify Smo as a bidirectional modulator of striatal DA-ACh coordination and striatal learning.

Introduction

Cholinergic interneurons (CIN) of the striatum play a critical role in action selection, associative learning, and behavioral flexibility (Morris, Arkadir et al. 2004, Joshua, Adler et al. 2008, Bertran-Gonzalez, Laurent et al. 2013, Bradfield, Bertran-Gonzalez et al. 2013, Okada, Nishizawa et al. 2014, Aoki, Liu et al. 2015, Maurice, Liberge et al. 2015, Matamales, Gotz et al. 2016). While recognized for their tonic pacemaker-like activity in the 5-10 Hz range, CIN also exhibit multi-phasic responses consisting of sustained pauses often flanked by bursts of activity in response to salient stimuli (Kimura, Rajkowski et al. 1984, Aosaki, Tsubokawa et al. 1994, Ravel, Legallet et al. 1999, Morris, Arkadir et al. 2004, Apicella, Ravel et al. 2011). These "conditioned pauses" (Schulz and Reynolds 2013, Zhang and Cragg 2017) develop throughout reinforcement learning and occur in anticorrelation with striatal dopamine (DA) release (Morris, Arkadir et al. 2004, Duhne, Mohebi et al. 2024).

The reductions in acetylcholine (ACh) produced by CIN pauses are thought to create a temporal window during which DA can modify corticostriatal synapses to drive learning (Kimura, Rajkowski et al. 1984, Aosaki, Graybiel et al. 1994, Graybiel, Aosaki et al. 1994, Morris, Arkadir et al. 2004). While glutamatergic input strength, intrinsic electrophysiological properties, and DA signaling have all been implicated in shaping CIN pauses (reviewed in (Ratna and Francis 2025)), CIN receive input from over 40 neuromodulatory systems—many of which remain poorly characterized (Lim, Kang et al. 2014, Ratna and Francis 2025). This complex signaling landscape likely further tunes CIN output and downstream striatal function (Lim, Kang et al. 2014, Zhang, Reynolds et al. 2018, Gallo, Greenwald et al. 2022, Martyniuk, Torres-Herraez et al. 2022, Ratna and Francis 2025).

Among these lesser-understood pathways, the secreted peptide Sonic Hedgehog (Shh) and its downstream effector—the GPCR Smoothened (Smo)—show the capacity to be critical modulators of CIN function. In particular, Shh signaling on CIN appears critical for long-term survival of both CIN and DA neurons (DAN) in mice (Ortega-de San Luis, Sanchez-Garcia et al. 2018), a finding supported by

human data from familial and sporadic cases of Parkinson's disease (PD) (Khan, Sobu et al. 2021, Schmidt, Luecken et al. 2022, Khan, Jaimon et al. 2024, Bagnoli, Lin et al. 2025, Lin, Jaimon et al. 2025).

Shh, expressed in the striatum by DAN and cortical layer 5 pyramidal tract (PTN) projections (Gonzalez-Reyes, Verbitsky et al. 2012, Harwell, Parker et al. 2012, Hobson, Choi et al. 2022, Russo, Pellegrino et al. 2024), is released in an activity-dependent manner (Petralia, Schwartz et al. 2011, Su, Yuan et al. 2017). Its receptor Patched (Ptch) is expressed in the striatum by CIN, Fast-Spiking Interneurons (FSI), and glia (Gonzalez-Reyes, Verbitsky et al. 2012), where it relieves Smo from cholesterol-mediated repression upon binding Shh (Zhang and Beachy 2023). Ptch and Smo localize to the primary cilium and postsynaptic compartments (Petralia, Schwartz et al. 2011, Petralia, Wang et al. 2012, Zhang and Beachy 2023), where Smo activation can trigger acute Gi-coupled signaling and slower Gli-dependent transcriptional changes (Bijlsma, Borensztajn et al. 2007, Arensdorf, Dillard et al. 2017, Zhang and Beachy 2023).

Beyond Shh maintaining CIN health, our prior work showed that Smo on CIN suppresses L-DOPA-induced dyskinesias (LID) (Malave, Zuelke et al. 2021), an aberrant form of motor learning caused by chronic levodopa treatment (Bastide, Meissner et al. 2015). This raises the question of whether—and how—Shh/Smo signaling contributes to CIN function in the healthy adult brain, particularly during periods of elevated DA, and whether it plays a role in coordinating DA-ACh interactions that underlie plasticity and motor learning.

Here, we show that Smo activity on CIN bidirectionally modulates DA-associated cholinergic inhibition in the dorsolateral striatum (DLS). Using cholinergic-specific manipulations, we demonstrate that dynamic Smo signaling is essential for organizing DA-ACh dynamics and for modulating both learning efficiency and behavioral adaptability.

RESULTS

Smo signaling on CIN modulates cholinergic inhibition following repeated dopaminergic stimulation

We previously found that ablation of Smo from CIN facilitates LID while expression of constitutive active SmoM2 on CIN attenuates LID formation and expression, and that administration of Smo agonist (SAG) increases CIN activity marker p-rpS6 while reducing dyskinesias dose- dependently and scaled with the L-Dopa dose used to elicit LID (Malave, Zuelke et al. 2021). These observations suggested an acute, functionally opposing interaction between Smo and DA receptor signaling on CIN. Given that D2 receptor signaling prolongs CIN pauses (Chuhma, Mingote et al. 2014, Straub, Tritsch et al. 2014, Gallo, Greenwald et al. 2022, Martyniuk, Torres-Herraez et al. 2022), we hypothesized that Smo signaling may counteract DA-mediated CIN inhibition. To test this, we manipulated Smo signaling and measured ACh levels during repeated optogenetic DA release in the DLS, a region critical for LID development (Girasole, Lum et al. 2018) and known for robust DA-associated CIN pauses (Duhne, Mohebi et al. 2024).

Control or $Smo^{L/L}$:$ChATCre^{+/-}$ mice with cholinergic-specific Smo ablation received AAV-Chrimson into the SNpc and AAV-GRAB DA or GRAB ACh sensors in the DLS along with an optic fiber for simultaneous photometry and stimulation (Fig. 1A, M). Given Smo modulates behavioral responses to repeated DA release over days (Malave, Zuelke et al. 2021), we performed the experiment for seven consecutive days.

Control mice showed consistent DA release with stimulation, unchanged by repetition or SAG (Fig. 1C-D). In GRAB ACh-expressing controls, DAN stimulation on day 1 evoked a several-second ACh dip. By day 7, this dip shortened and was followed by a rebound, consistent with conditioned pauses from local CIN rather than hindbrain cholinergic projections (Fig. 1E) (Martyniuk, Torres-Herraez et al. 2022, Krok, Maltese et al. 2023). In $Smo^{L/L}$:$ChATCre^{+/-}$ mice, ACh dips were similar on day 1 but

unchanged across sessions, lacking rebound and differing significantly from controls by day 7 (Fig. 1F-H).

Acute Smo activation on CIN modulates cholinergic inhibition

To test whether acute Smo signaling modulates CIN inhibition, we repeated stimulation with SAG administered 30 minutes prior (Fig. 1B, I-J). SAG-treated controls showed reduced dip duration and rebound latency in early sessions compared to untreated controls, indicating acute Smo involvement (Fig. 1K-L). These effects plateaued by the final session, suggesting saturation of the effect. SAG-treated $Smo^{L/L}$:$ChATCre^{+/-}$ mice showed no changes, indicating CIN autonomous Smo-dependent modulation.

Ablation of Smo from CIN enhances cholinergic inhibition coincident with endogenous DA release

To test if these Smo-dependent effects occur under natural DA signaling, we recorded spontaneous ACh/DA release in head-fixed $Smo^{L/L}$:$ChATCre^{+/-}$ and $Smo^{L/+}$:$ChATCre^{+/-}$ littermates co-infused with GRAB ACh and DA sensors (Fig. 2A-B). Animals were habituated atop a running wheel inside a light-proof cabinet and recorded for 30 minutes (Fig 2C). To detect spontaneous cholinergic activity in the absence of a behavioral task, we applied a 3-median absolute deviation (MAD) threshold to the GRAB ACh signal, defining suprathreshold events and their aligned DA traces as "ACh Events" (Fig. 2A; see Methods). Session-averaged traces reflected previously-described anticorrelated ACh/DA patterns (Fig. 2A; Session Average). ACh Event rates were similar between genotypes (Supplementary Fig. 1A), but comparison of ACh Event profiles revealed a genotype x time interaction, suggesting differences in profile features (Fig. 2D).

We segmented ACh Events into three features: Focal Event, Post Event Inhibition, and Recovery from Maximal Inhibition. However, these revealed no clear differences between genotypes (Fig. 2E-F). Guided by our observations that Smo preferentially influences CIN during periods of elevated DA such as DAN stimulation or L-DOPA treatment, we next ranked all ACh Events by their coincident DA levels and compared averages of those from the top and bottom terciles of coincident-DA levels (Fig. 2G;

Supplementary Fig. 2). This approach revealed that under high-DA conditions, $Smo^{L/L}$:$ChATCre^{+/-}$ mice showed stronger Post-Event Inhibition and weaker Recovery compared to controls (Fig. 2G-H; Supplementary Fig. 3B). Realignment of Events to Post-Event Inhibition onset revealed that this effect was driven by prolonged inhibition in mutants (Fig. 2I-K).

Including $ChATCre^{+/-}$ controls with two intact Smo alleles strengthened the observed effect on dip duration (Supplemental Fig. 4E). Thus, Smo modulates duration and recovery of CIN pauses in response to physiologic DA fluctuations.

SmoM2 expression on CIN opposes cholinergic inhibition coincident with endogenous DA release

To complement these loss-of-function results, we expressed constitutively active SmoM2 on CIN ($SmoM2^{C/-}$:$ChATCre^{+/-}$). As with $Smo^{L/L}$:$ChATCre^{+/-}$ animals, pre-stratification profiles were comparable to controls (Supplementary Fig. 5). However, under high-coincident DA, SmoM2 animals resisted inhibition with shorter Post-Event Inhibitions and less dampened recovery (Fig. 2L-O; Supplementary Fig. 3C-D). These loss- and gain-of-function results indicate that Smo signaling modulates CIN pause duration coincident with elevated DA in a bidirectional and graded manner.

Multivariate analysis of changes in ACh signaling due to Smo on CIN

To fully assess the effect of Smo manipulations on ACh Event features, we performed principal component analysis (PCA) on 51 parameters across all ACh Events. In both $Smo^{L/L}$:$ChATCre^{+/-}$ and $SmoM2^{C/-}$:$ChATCre^{+/-}$ datasets, PC1 captured ~17-20% of variance and differed significantly by genotype despite overlap (Supplementary Fig. 6 C-D). Key contributors included Post-Event Inhibition and Rebound dynamics. In both datasets, parameter #23—the relative Post-Event Inhibition to Focal Event magnitude—had the strongest loading ($\leq$-0.87). Across datasets, reduced Smo signaling correlated with negative PC1 scores while elevated Smo shifted scores positively. This multivariate approach further supports our observations that Smo on CIN modulates ACh inhibition in a subset of ACh Events.

Smo contributes to the organization of ACh-DA dynamics

DA and ACh signals are anticorrelated and phase-shifted across behavioral states (Fig. 2A; (Krok, Maltese et al. 2023). We therefore examined whether Smo shapes this temporal coordination by computing cross-correlations between DA and ACh photometry signals centered on ACh Events (Fig. 3A). Three prominent correlations emerged from this analysis: a negative one at -50ms (peak 1; degree to which DA dip predicts ACh Event), and positive ones at -200ms (peak 2; degree to which DA release predicts ACh inhibition recovery), and +200ms (peak 3; degree to which ACh Event predicts DA release).

$Smo^{L/+}$:$ChATCre^{+/-}$ and $Smo^{L/L}$:$ChATCre^{+/-}$ animals showed delayed peak 1 and 2 timing without changes in correlation strength, suggesting slowed but not weakened ACh responsiveness to DA (Fig. 3A-C; top). In contrast, $SmoM2^{C/-}$:$ChATCre^{+/-}$ mice showed broad disruption of all cross-correlation peaks (Fig. 3A-C; Supplementary Fig. 7; bottom). Notably, peak 2 timing was again altered without a change in correlation strength—but in the opposite direction to that observed in $Smo^{L/L}$:$ChATCre^{+/-}$ mice, highlighting a bidirectional effect of Smo on DA-ACh coordination.

Smo modulates the dynamic range of striatal ACh

CIN activity maintains tonic ACh levels, enabling bidirectional deviations from baseline. To assess how Smo manipulations affected this dynamic range, we plotted the percentage of samples across deviation magnitudes from the session average. $Smo^{L/L}$:$ChATCre^{+/-}$ mice revealed a broadening of the distribution with fewer values around the mean and at the tails compared to controls (Fig. 3E, G-H). In contrast, $SmoM2^{C/-}$:$ChATCre^{+/-}$ mice showed an opposite, though nonsignificant, trend of sharpening the distribution with increased representation of values around the mean (Fig. 3F-H; bottom). These findings suggest that dynamic Smo signaling helps preserve the full range of ACh fluctuations, while static gain- or loss-of-function may constrain it.

Smo on CIN bidirectionally modulates motor learning

To test the behavioral relevance of these Smo manipulations on striatal behaviors, we trained mice on a rotarod with accelerating and holding phases. Learning criterion was defined as reaching top

speed on more than 50% of trials in a day and the slopes of performance to this point were compared (Fig. 4A-B). $Smo^{L/L}$:$ChATCre^{+/-}$ mice reached criterion sooner than controls while $SmoM2^{C/-}$:$ChATCre^{+/-}$ animals exhibited the opposite trend (Fig. 4C-F). When mutant performance was normalized to respective controls and directly compared, the opposing effects were accentuated, highlighting a bidirectional effect (Fig. 4G). Post-criterion performance in which animals routinely reached the holding phase showed no differences, highlighting an effect on learning rate (Fig. 4 H).

Smo on CIN modulates striatal reinforcement learning

To assess whether Smo ablation affects reinforcement learning, we trained $Smo^{L/L}$:$ChATCre^{+/-}$ and control mice to lever press on an escalating random interval (RI) schedule (Fig. 4I; see Methods). Although both groups showed similar reward acquisition and total pressing (Fig. 4I, J), only controls exhibited sensitivity to reward devaluation after three days of RI15 training (Fig. 4K) Press-timing analysis of the day prior to devaluation revealed that controls tended to front-load responses, while mutants displayed more uniform press distributions (Fig. 4L), suggesting reduced within-session adaptation. This diminished flexibility was reflected on the first day of RI30 training, where controls but not mutants increased inter-press interval variance—consistent with within-session exploration of pressing strategies. Continued RI30 training revealed two general strategies among mice: isolated lever presses or grouped bouts of presses interleaved with magazine checks. While control animals maintained a consistent ratio of single to bout presses, $Smo^{L/L}$:$ChATCre^{+/-}$ mutants showed a marked shift toward bout-dominant responding (Fig. 4N, O), with average bout size also increasing over time (Fig. 4P).

These results led us to examine whether Smo ablation from CIN would modify performance on a Progressive Ratio (PR) task where action-reward contingencies constantly change and each reward requires twice as many presses as the last. In a single 2hr session, mutants again showed uniform responses, with delayed distribution of effort (Supplementary Fig. 8A-B). These findings suggest Smo ablation from cholinergic neurons enhances stereotyped and outcome-insensitive reinforced behavior.

Discussion

The mechanisms coordinating DA and ACh release in the striatum remain unclear, but their interaction—whether direct or via shared inputs—is crucial for learning. Here, we identify the atypical GPCR Smo, an effector of the Shh pathway, as a modulator of this coordination and its behavioral consequences. Specifically, enhanced Smo activity attenuated ACh inhibition during periods of elevated DA, while Smo loss prolonged inhibition and prevented its progressive shortening with repeated DAN stimulation. Smo manipulations also bidirectionally shifted the timing of ACh-DA correlations and constrained ACh's dynamic range. Consistent with these physiological effects, Smo ablation accelerated motor learning but impaired behavioral flexibility.

Smo activity on CIN opposes DA-dependent pause prolongation and rebound suppression

Elevated Smo signaling shortened the pause and promoted rebound activity—features known, in part, to be regulated by D2 signaling on CIN (Gallo, Greenwald et al. 2022, Martyniuk, Torres-Herraez et al. 2022). The bidirectional effects of Smo on these features was evident across two paradigms: optogenetic DAN stimulation and physiologically occurring DA/ACh fluctuations. In the former, Smo altered pause-rebound dynamics both acutely and progressively across repeated daily stimulations, implicating short- and long-term mechanisms. In the latter, focused on a subset of prominent spontaneous ACh Events—likely driven by cortical excitation of CIN (Kosillo, Zhang et al. 2016, Krok, Maltese et al. 2023)—Smo modulated pause duration during coincident DA surges. Together, these findings suggest Smo tunes CIN pause-rebound dynamics in DA-associated contexts.

Shh signaling within the striatal circuit

Smo is indirectly activated by Shh (Zhang and Beachy 2023), which is expressed in the striatum by PTN and DAN (Gonzalez-Reyes, Verbitsky et al. 2012, Harwell, Parker et al. 2012, Hobson, Choi et al. 2022, Russo, Pellegrino et al. 2024). Thus, either input could engage Smo on CIN primary cilia or

synapses. Supporting this, serial EM tomography shows how primary cilia—key in Shh signaling and present on CIN—can form synapses with adjacent axons (Wu, Cho et al. 2024). Shh signaling drives concentration-dependent transcriptional and second-messenger responses (Zhang and Beachy 2023), aligning with the progressive and acute effects of Smo modulation we observed on CIN, and allowing for potential integration of multiple input sources of Shh.

FSI also express Smo and are known to inhibit CIN, suggesting Shh may modulate circuit dynamics both by direct disinhibition and indirect inhibition of ACh. CIN activity can spread across the dorsal striatum in form of traveling Turing waves (Matityahu, Gilin et al. 2023). Shh/Smo signaling can impact morphogenesis during development as a component of Turing wave-forming reaction-diffusion systems (Menshykau, Blanc et al. 2014, Delgado and Torres 2016, Pickering and Towers 2016, Cooper, Jahanbakhsh et al. 2025). While speculative, it is intriguing to consider that Smo-dependent modulation of FSI-CIN microcircuits could influence both the propagation and termination of ACh waves.

Smo signaling on CIN impacts striatal behaviors

The triphasic CIN response is linked to striatal learning (Schulz and Reynolds 2013, Straub, Tritsch et al. 2014, Kim, Capps et al. 2019). Consistent, our behavioral findings paralleled physiological observations, suggesting that Smo manipulations bidirectionally affect rotarod learning. In an operant task, Smo ablation also potentiated initial learning but impaired sensitivity to changing action-outcome contingencies. These results align with models proposing he DLS encodes stimulus-action associations that streamline performance and promote habit formation, as well as with models of corticostriatal plasticity in which ACh dips coinciding with DA release define a temporal window for synaptic plasticity. Loss of Smo may therefore promote outcome-insensitive behaviors by prolonging CIN pauses in the DLS and widening this plasticity window.

Implications for striatal disease

Shh/Smo signaling maintains mesostriatal health and buffers CIN from excessive DA inhibition in LID models (Ortega-de San Luis, Sanchez-Garcia et al. 2018, Malave, Zuelke et al. 2021). Recently, reduced CIN-specific Smo signaling was also associated with familial and sporadic forms of PD (Khan, Sobu et al. 2021, Bagnoli, Lin et al. 2025, Lin, Jaimon et al. 2025). Our findings extend these observations to the intact brain, identifying Smo as a modulator of DA–ACh coordination during learning. This suggests that early disruptions in Shh/Smo signaling may impair striatal plasticity before overt neurodegeneration emerges. In this view, physiological fluctuations in Smo activity that support adaptive learning may, if unregulated, contribute to pathological circuit remodeling, highlighting a potential mechanism linking early synaptic dysfunction to later degeneration in basal ganglia disorders.

Limitations of the study

A primary limitation of this study is the absence of simultaneous cholinergic recordings during behavior. However, the use of the same genetic models in which dorsolateral CIN pause dynamics were altered, combined with a focus on DLS-dependent behaviors, supports a role for CIN-specific Smo signaling in shaping behavioral output.

A second limitation is that $Smo^{L/L}$:$ChATCre^{+/-}$ and $SmoM2^{C/-}$:$ChATCre^{+/-}$ mice are maintained on different background strains (see Methods). Although bidirectional effects were observed across analyses, and appropriate littermate controls, alternate controls, and within-subject pharmacological manipulations were employed, background specific differences may have masked the full range of Smo gain- and loss-of-function.

Despite these caveats, our findings indicate that Smo signaling on CIN shapes pause-rebound dynamics, DA-ACh coordination, and striatal learning. These functions may represent early sites of dysfunction in basal ganglia disorders, offering insights into both normal learning and prodromal stages of disease.

Main Figure Legends

Figure 1. Smo on CIN modulates ACh inhibition following repeated DAN stimulation

(A) *Left:* Viral strategy for simultaneous DAN terminal stimulation and GRAB ACh or DA recording in DLS. *Right:* Representative traces across four laser pulse trains with session averages.

(B) Daily stimulation protocol in ChATCre$^{+/-}$ or Smo$^{L/L}$:ChATCre$^{+/-}$ mice ±SAG.

(C) DA signal aligned to laser onset on day 1 and 7 in ChATCre$^{+/-}$ mice (n = 7). 20 Mg/Kg SAG administered on day 8.

(D) DA release AUC quantified from (C) (n = 7; one-way ANOVA: ns).

(E) ACh signal on days 1 and 7 in ChATCre$^{+/-}$ mice (n = 7). Two-way ANOVA: time, $F(1966,11796) = 21.48$, $p < 0.0001$; day, $F(1,6) = 8.26$, $p < 0.05$; interaction, $F(1966, 11796) = 5.54$, $p < 0.0001$; Šídák's: ****$p < 0.0001$.

(F) Same as (E) in Smo$^{L/L}$:ChATCre$^{+/-}$ mice (n = 6).

(G) Dip duration (n = 6-7). Two-way ANOVA: day, $F(1,11) = 7.12$, $p < 0.05$; LSD: *$p < 0.05$, **$p < 0.01$.

(H) Rebound duration. Two-way ANOVA: day, $F(1,11) = 7.12$, $p < 0.05$; genotype, $F(1, 11) = 7.731$, $p < 0.05$; LSD: **$p < 0.01$.

(I-J) ACh signal in SAG-treated mice (n = 7-8).

(K) Dip duration across days ±SAG. ChATCre$^{+/-}$ Two-way ANOVA: day, $F(3.491,45.39) = 4.81$, $p < 0.01$; pharmacology, $F(1,13) = 5.52$, $p < 0.05$; Tukey's: *$p < 0.05$. Smo$^{L/L}$:ChATCre$^{+/-}$ Two-way ANOVA: ns.

(L) Timing of max rebound across days ±SAG. ChATCre$^{+/-}$ Two-way ANOVA: day, $F(3.327,43.26) = 4.50$, $p < 0.01$; pharmacology, $F(1,13) = 5.22$, $p < 0.05$; Tukey's: *$p < 0.05$. Smo$^{L/L}$:ChATCre$^{+/-}$ Two-way ANOVA: day: ns.

(M) GRAB sensor and ChrimsonR-tdTomato expression in DLS and SNpc. Scale bar = 500µm.

Figure 2. CIN Smo bidirectionally modulates ACh inhibition in response to endogenous DA levels

(A) *Left*: Viral strategy for simultaneous GRAB ACh and DA recordings in DLS. *Right*: Representative traces from a single mouse, with session-averaged ACh Event-aligned profiles.

(B) GRAB sensor expression in the striatum. Scale bar = 500µm.

(C) Recording protocol for control, $Smo^{L/L}$:$ChATCre^{+/-}$, and $SmoM2^{C/-}$:$ChATCre^{+/-}$ mice.

(D) Replicate and genotype-grouped ACh Events (n = 7-9). Two-way ANOVA: time, $F(1.167,16.34) = 29.77$, $p < 0.0001$; interaction, $F(698,9772) = 4.19$, $p < 0.0001$.

(E) Quantified ACh Event features.

(F) Average z-scores for features in (E) (n = 7-9). Unpaired t-test: ns.

(G) ACh Events grouped by coincident DA levels (n = 7-9).

(H) Recovery from Maximal Inhibition. Two-way ANOVA: DA, $F(1,14) = 4.18$, $p = 0.06$; interaction, $F(1,14) = 3.43$, $p = 0.085$; LSD: *$p < 0.05$.

(I-J) ACh Events realigned to Post-Event Inhibition onset.

(K) Post-Event Inhibition duration (n = 7-9). Two-way ANOVA: genotype, $F(1,14) = 6.01$, $p < 0.05$; LSD: *$p < 0.05$.

(L-M) Same analysis in $SmoM2^{C/-}$:$ChATCre^{+/-}$ (n = 8-10). Two-way ANOVA: DA, $F(1,16) = 8.02$, $p < 0.05$; LSD: *$p < 0.05$.

(N-O) Realigned ACh Events and Inhibition duration by DA level. Two-way ANOVA: interaction, $F(1,16) = 4.15$, $p = 0.06$; LSD: *$p < 0.05$.

Figure 3. CIN Smo is required for normal ACh dynamics and DA coordination

(A) Average cross-correlation between ACh and DA signals aligned to ACh Events. Numbered peaks correspond to (B-C).

(B) Minimum correlation at negative lag. *Left*: Coefficient; *Right*: timing. *Top:* $Smo^{L/L}$:$ChATCre^{+/-}$ (n = 7-9). One-way ANOVA: timing, $p < 0.05$; Tukey's: *$p < 0.05$. *Bottom:* $SmoM2^{C/-}$:$ChATCre^{+/-}$ (n = 8-10). Unpaired t-test: ns.

(C) Maximum correlation at negative lag. $Smo^{L/L}$:$ChATCre^{+/-}$ One-way ANOVA: timing, $p < 0.05$; Tukey's: **$p < 0.01$. $SmoM2^{C/-}$:$ChATCre^{+/-}$ Unpaired t-test: *$p < 0.05$.

(D) Representative GRAB ACh traces.

(E-F) Distribution of ACh values relative to session average. *Inset:* interquartile ranges. (E) $Smo^{L/L}$:$ChATCre^{+/-}$ (n = 7-9). One-way ANOVA: $p < 0.01$; Tukey's: **$p < 0.01$. (F) $SmoM2^{C/-}$:$ChATCre^{+/-}$ (n = 8-10). Unpaired t-test: ns.

(G) Percent of ACh values binned by absolute deviation (0.1 z-score bins). *Top*: $Smo^{L/L}$:$ChATCre^{+/-}$ Two-way ANOVA: deviation, $F(14,308) = 98.40$, $p < 0.0001$; Šídák's: ****$p < 0.0001$, **$p < 0.01$, *$p < 0.05$. *Bottom*: $SmoM2^{C/-}$:$ChATCre^{+/-}$ Two-way ANOVA: deviation, $F(14,224) = 39.65$, $p < 0.0001$.

(H) Percent ACh values with |deviation| >0.5. *Top*: $Smo^{L/L}$:$ChATCre^{+/-}$ One-way ANOVA: $p < 0.05$. *Bottom*: $SmoM2^{C/-}$:$ChATCre^{+/-}$ Mann-Whitney: ns.

Figure 4. Behavioral effects of genetic Smo manipulations on CIN

(A) Rotarod trial structure (10x/day).

(B) Latency to fall and best-fit learning slopes for $Smo^{L/L}$:$ChATCre^{+/-}$ (n = 8), $SmoM2^{C/-}$:$ChATCre^{+/-}$ (n = 9-10), and controls.

(C-F) Slope and days to criterion. Unpaired t-test: *$p < 0.05$.

(G-H) Learning slope and post-criterion performance normalized to background strain (n = 8-10). Unpaired t-test: **$p < 0.01$.

(I-J) Lever presses and rewards across escalating RI training (n = 8-12).

(K) Reward devaluation pressing (*Left:* Two-way ANOVA: devaluation, $F(1,18) = 16.72$, $p < 0.001$; LSD: ***$p < 0.001$) and magazine entries (*Right:* Two-way ANOVA: devaluation, $F(1,18) = 43.31$, $p < 0.0001$; LSD: ****$p < 0.0001$, ***$p < 0.001$).

(L) Cumulative press distribution and total presses (*inset*) on final RI15 day.

(M) Inter-press interval coefficient of variation. Two-way ANOVA: interaction, $F(1,18) = 3.27$, $p = 0.08$; LSD: *$p < 0.05$.

(N) Example behavior from RI30 training.

(O-P) Press strategies across RI30 training: bout preference (Two-way ANOVA: day, $F(1,18) = 7.98$, $p < 0.05$; LSD: $^*p < 0.05$) and size (Two-way ANOVA: day: $F(1,18) = 6.34$, $p < 0.05$; LSD: $^*p < 0.05$).

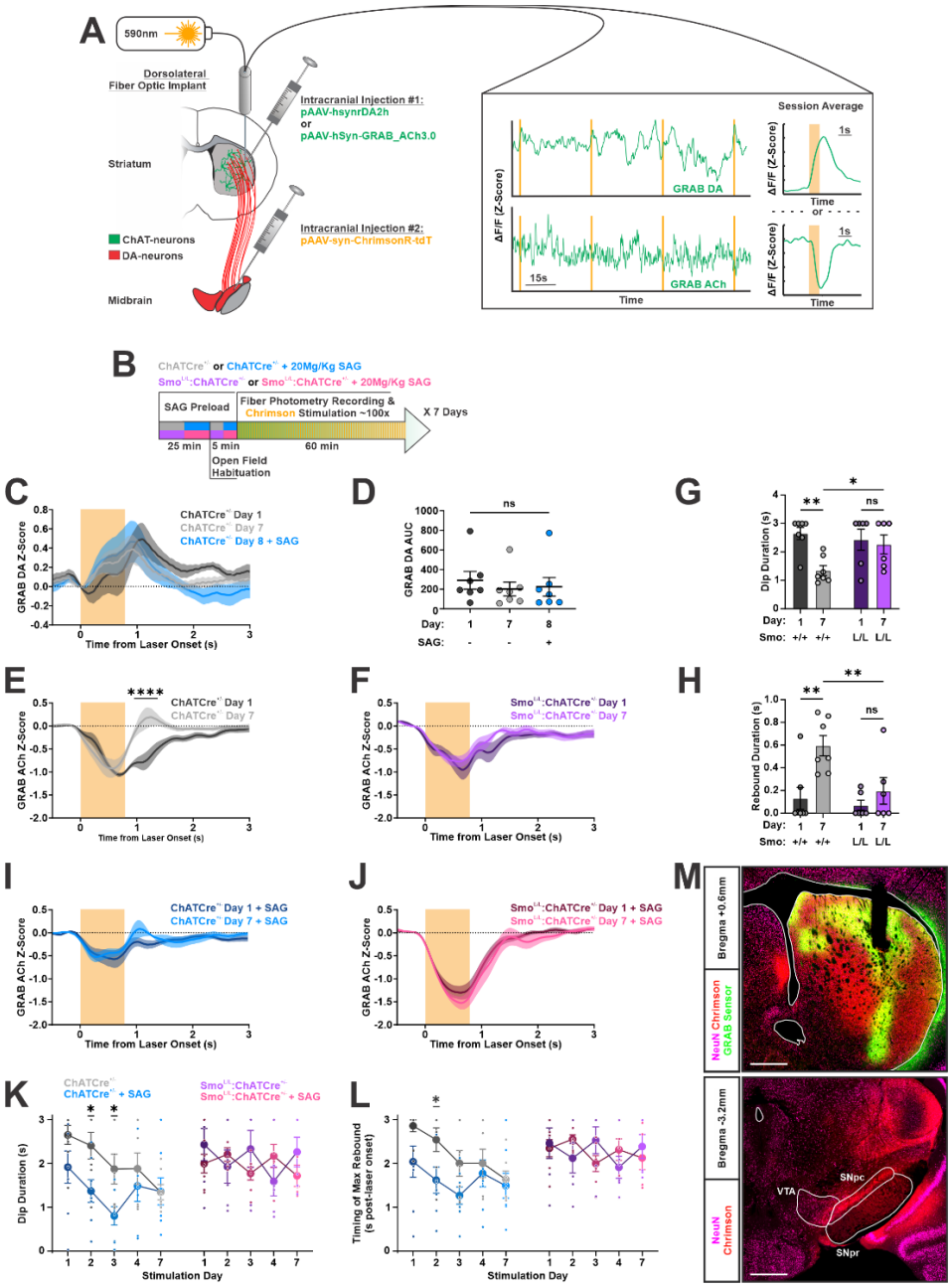
A
590nm
Dorsolateral Fiber Optic Implant
Striatum
ChAT-neurons
DA-neurons
Midbrain
Intracranial Injection #1:
pAAV-hsynrDA2h
or
pAAV-hSyn-GRAB_ACh3.0
Intracranial Injection #2:
pAAV-syn-ChrimsonR-tdT
Session Average
GRAB DA
GRAB ACh
ΔF/F (Z-Score)
Time
15s
1s
or
B
SAG Preload
Fiber Photometry Recording & Chrimson Stimulation ~100x
X 7 Days
25 min
5 min
60 min
Open Field Habituation
C
GRAB DA Z-Score
Time from Laser Onset (s)
D
GRAB DA AUC
ns
Day:
SAG:
G
Dip Duration (s)
Smo:
E
GRAB ACh Z-Score
F
H
Rebound Duration (s)
I
J
M
Bregma +0.6mm
Bregma -3.2mm
NeuN Chrimson GRAB Sensor
NeuN Chrimson
VTA
SNpc
SNpr
K
Dip Duration (s)
Stimulation Day
L
Timing of Max Rebound (s post-laser onset)

Figure 1

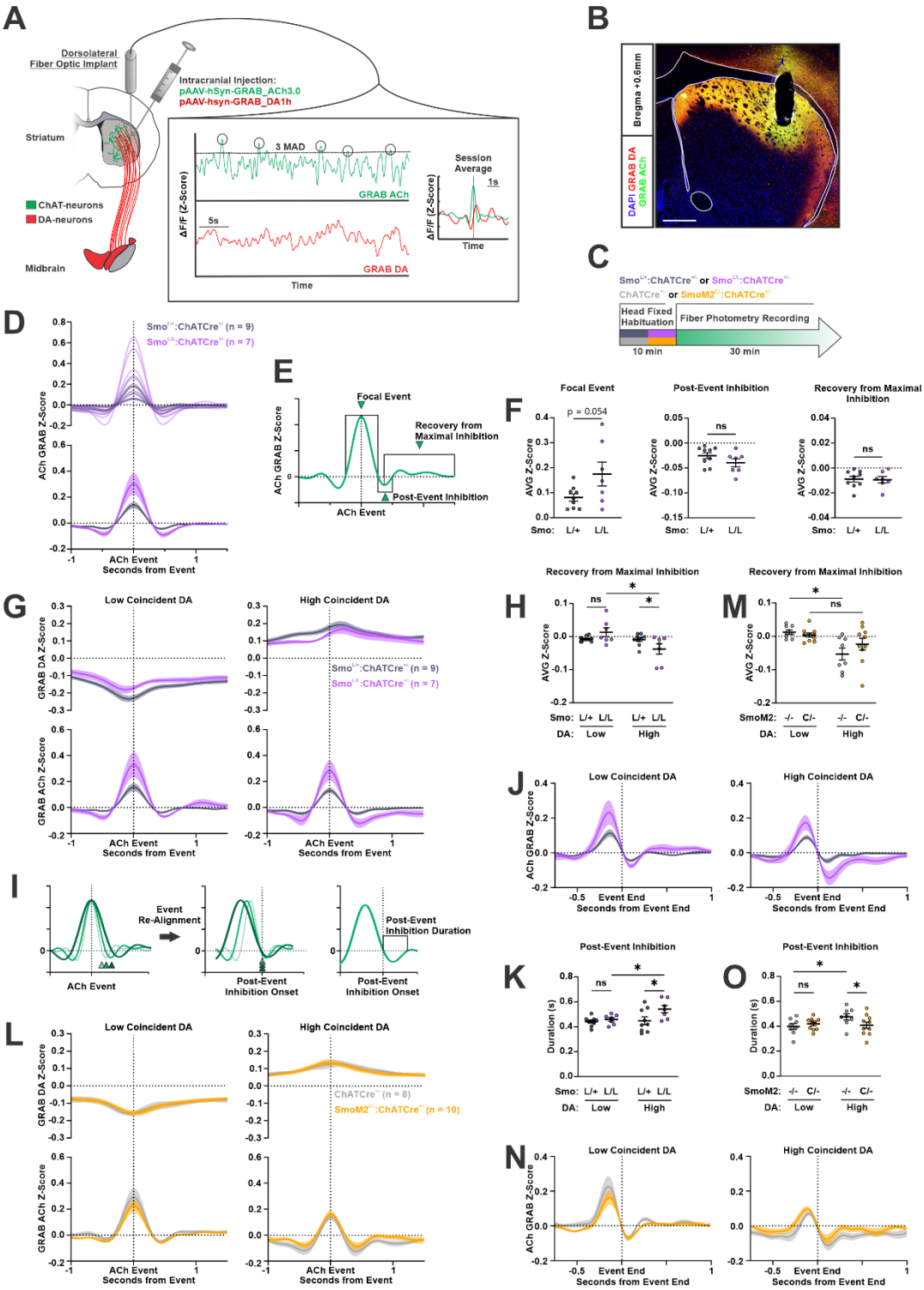
A
Dorsolateral Fiber Optic Implant
Intracranial Injection:
pAAV-hSyn-GRAB_ACh3.0
pAAV-hsyn-GRAB_DA1h
Striatum
ChAT-neurons
DA-neurons
Midbrain
3 MAD
GRAB ACh
5s
GRAB DA
ΔF/F (Z-Score)
Time
Session Average
1s
B
Bregma +0.6mm
DAPI GRAB DA GRAB ACh
C
Head Fixed Habituation
Fiber Photometry Recording
10 min
30 min
D
ACh GRAB Z-Score
ACh Event
Seconds from Event
E
Focal Event
Recovery from Maximal Inhibition
Post-Event Inhibition
F
Focal Event
Post-Event Inhibition
Recovery from Maximal Inhibition
AVG Z-Score
p = 0.054
ns
Smo:
G
Low Coincident DA
High Coincident DA
GRAB DA Z-Score
GRAB ACh Z-Score
H
M
Recovery from Maximal Inhibition
DA:
Low
High
SmoM2:
I
Event Re-Alignment
Post-Event Inhibition Onset
Post-Event Inhibition Duration
J
Event End
Seconds from Event End
K
O
Post-Event Inhibition
Duration (s)
L
N

Figure 2

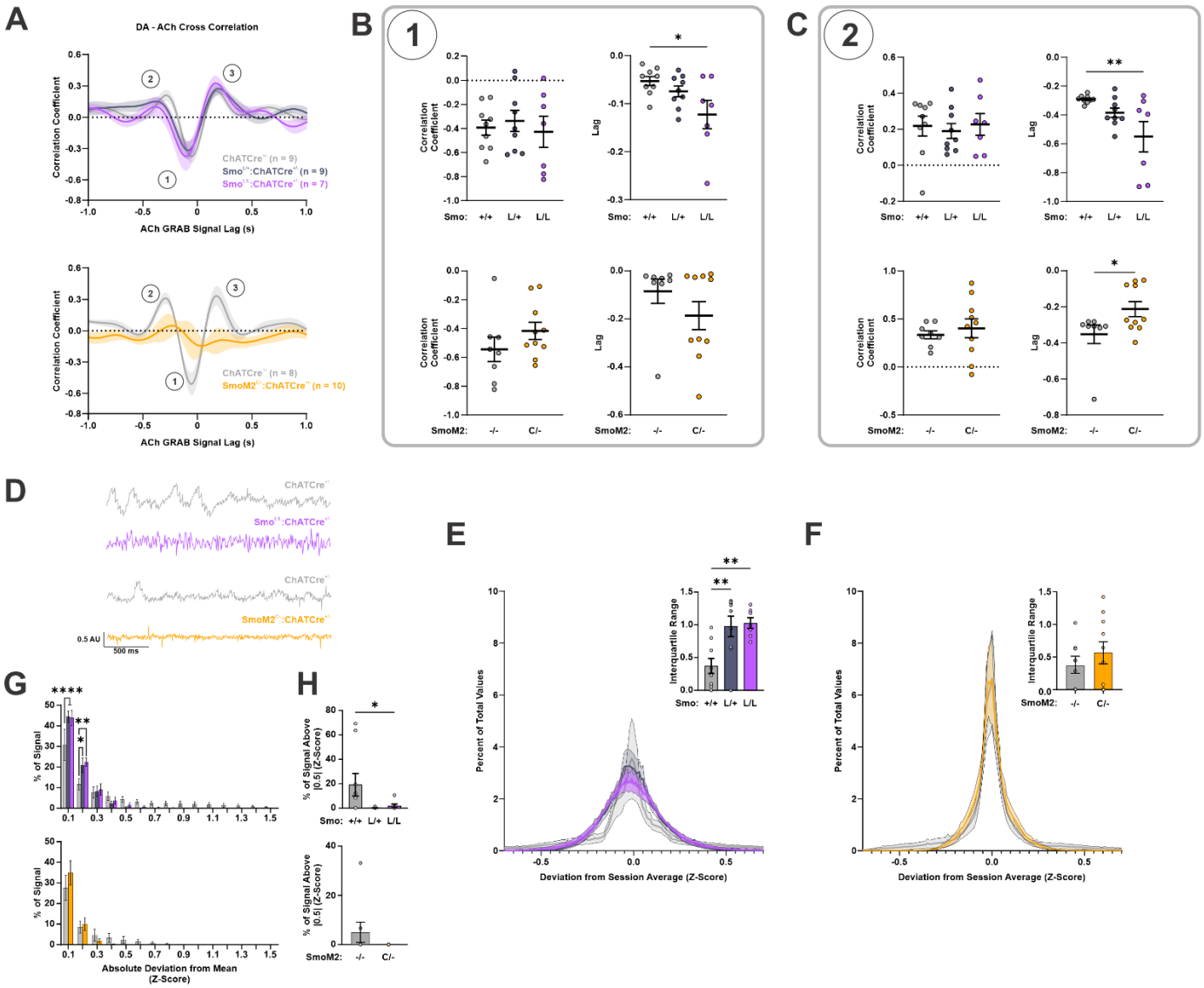
A
DA - ACh Cross Correlation
Correlation Coefficient
ACh GRAB Signal Lag (s)
ChATCre⁻⁻ (n = 9)
Smo⁺/⁺:ChATCre⁺⁺ (n = 9)
Smo⁺/⁺:ChATCre⁺⁺ (n = 7)
ChATCre⁻⁻ (n = 8)
SmoM2⁻/⁻:ChATCre⁺⁺ (n = 10)
B
1
Correlation Coefficient
Lag
Smo: +/+ L/+ L/L
SmoM2: -/- C/-
C
2
D
ChATCre⁺⁺
Smo⁺/⁺:ChATCre⁺⁺
SmoM2⁻/⁻:ChATCre⁺⁺
0.5 AU
500 ms
E
Percent of Total Values
Deviation from Session Average (Z-Score)
Interquartile Range
F
G
% of Signal
Absolute Deviation from Mean (Z-Score)
H
% of Signal Above |0.5| (Z-Score)

Figure 3

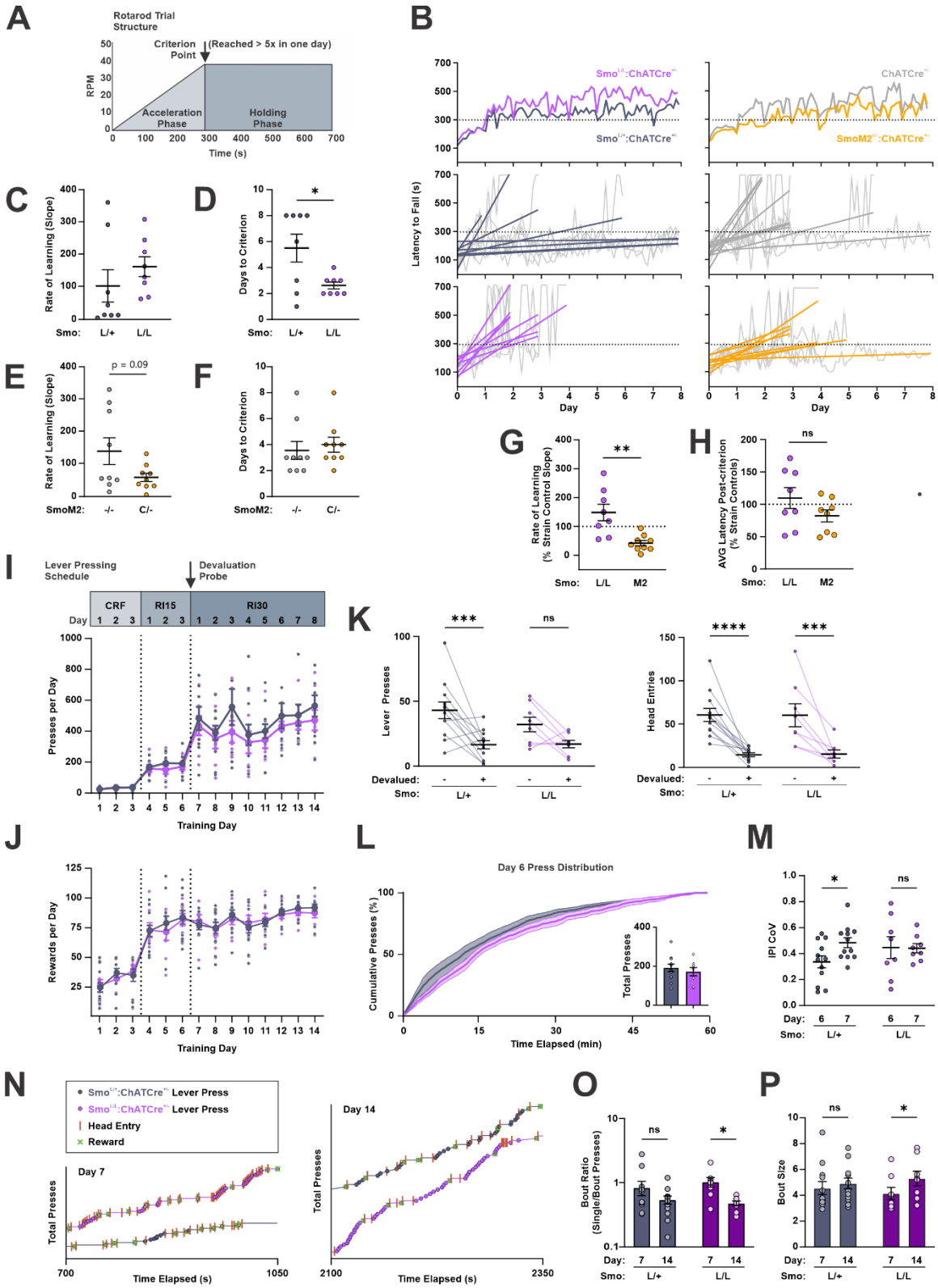
A
Rotarod Trial Structure
Criterion Point
(Reached > 5x in one day)
RPM
Acceleration Phase
Holding Phase
Time (s)
B
Latency to Fall (s)
Day
C
Rate of Learning (Slope)
Smo: L/+ L/L
D
Days to Criterion
E
p = 0.09
SmoM2: -/- C/-
F
G
Rate of Learning (% Strain Control Slope)
Smo: L/L M2
H
ns
AVG Latency Post-criterion (% Strain Controls)
I
Lever Pressing Schedule
Devaluation Probe
CRF
RI15
RI30
Presses per Day
Training Day
K
Lever Presses
Devalued:
Smo:
Head Entries
J
Rewards per Day
L
Day 6 Press Distribution
Cumulative Presses (%)
Time Elapsed (min)
Total Presses
M
IPI CoV
Day:
N
Lever Press
Head Entry
Reward
Day 7
Day 14
Time Elapsed (s)
O
Bout Ratio (Single/Bout Presses)
P
Bout Size

Figure 4

Supplementary Figure Legends

Supplementary Figure 1. Frequency of significant ACh Events across genotypes

Frequency of ACh Events detected using a 3MAD thresholding method (see Methods).

(A) $Smo^{L/L}$:$ChATCre^{+/-}$ mice versus controls (n = 7-9). One-way ANOVA: ns.

(B) $SmoM2^{C/-}$:$ChATCre^{+/-}$ mice versus controls (n = 8-10). Mann-Whitney: *p <0.05.

Supplementary Figure 2. Stratification of ACh Events by levels of coincident DA

(A) ACh Events and coincident DA values from control mice, grouped by animal and ranked by ACh Event magnitude.

(B) Same as (A) for $Smo^{L/L}$:$ChATCre^{+/-}$ mice.

(C) All ACh Events from control mice grouped and ranked by the magnitude of coincident DA. Events were then stratified into high, middle, and low tiers of coincident DA.

(D) Same as (C) for $Smo^{L/L}$:$ChATCre^{+/-}$ mice.

(E) ACh Event-DA pairs from high and low DA tiers regrouped by mouse to derived new animal-level averages. Within-animal traces are ranked by coincident DA.

(F) Same as (E) for $Smo^{L/L}$:$ChATCre^{+/-}$ mice.

Supplementary Figure 3. Effects of Smo manipulations on ACh Event Focal Event and Post-Event Inhibition under high and low coincident DA levels

(A) Average ACh Focal Event z-scores for DA-stratified control and $Smo^{L/L}$:$ChATCre^{+/-}$ traces (Fig. 2G; n = 7-9). Two-way ANOVA: DA, $F(1,14) = 4.88$, $p < 0.05$; LSD: *$p < 0.05$.

(B) Same as (A), for Post-Event Inhibition. Two-way ANOVA: genotype, $F(1,14) = 6.35$, $p < 0.05$; LSD: *$p < 0.05$.

(C) Average ACh Focal Event z-scores for DA-stratified control and $SmoM2^{C/-}$:$ChATCre^{+/-}$ traces (Fig. 2L; n = 8-10). Two-way ANOVA: DA, $F(1,16) = 8.29$, $p < 0.05$; LSD: *$p < 0.05$.

(D) Same as (C), for Post-Event Inhibition. Two-way ANOVA: DA, $F(1,16) = 4.97$, $p < 0.05$; LSD: *$p < 0.05$.

Supplementary Figure 4. Ablation of Smo from CIN alters DA-associated ACh inhibition relative to alternate homozygous controls

(A) Genotype averaged ACh Events for ChATCre$^{+/-}$ control and Smo$^{L/L}$:ChATCre$^{+/-}$ mice (n = 7-9). Two-way ANOVA: time, $F(1.275,17.86) = 21.02$, $p < 0.001$; genotype, $F(1,14) = 4.63$, $p < 0.05$; interaction, $F(698,9772) = 1.89$, $p < 0.0001$.

(B) Same ACh Events stratified by relative levels of coincident DA (n = 7-9).

(C) Average z-scores for ACh Event features extracted from (B). *Left*: Focal Event. Two-way ANOVA: DA, $F(1,14) = 2.66$, $p > 0.05$; LSD: *$p < 0.05$. *Middle*: Post-Event Inhibition. Two-way ANOVA: DA, $F(1,14) = 1.32$, $p > 0.05$. *Right*: Recovery from Post-Event Inhibition. Two-way ANOVA: DA, $F(1,14) = 5.02$, $p < 0.05$.

(D) ACh Events realigned and segregated by coincident DA level (n = 7-9).

(E) Duration of Post-Event Inhibition isolated from traces in (D). Two-way ANOVA: DA, $F(1,14) = 6.42$, $p < 0.05$; genotype, $F(1,14) = 12.43$, $p < 0.001$; LSD: ***$p < 0.001$, *$p < 0.05$.

Supplementary Figure 5. Comparison of unstratified SmoM2 ACh Events

(A) *Top*: Session-averaged ACh Events from individual control and SmoM2$^{C/-}$:ChATCre$^{+/-}$ mice. *Bottom*: Genotype averages (n = 8-10). Two-way ANOVA: time, $F(1.967,31.47) = 93.78$, $p < 0.0001$; interaction, $F(700,11200) = 2.20$, $p < 0.0001$.

(B) Average ACh z-scores (± SEM) for features extracted from traces in (A) (n = 8-10). Unpaired t-test: ns.

Supplementary Figure 6. Principal component analysis of ACh Events in Smo loss- and gain-of-function models

(A) Schematic of representative ACh Event with color-coded arrows denoting features used in analysis and corresponding to (B). All features begin and end at baseline (dashed vertical lines).

(B) List of parameters used in principal component analysis (PCA), grouped by feature type. Color-coded labels match features in (A). Colons indicate segments defined between specific features.

(C) *Left*: PC scores for individual ACh Events from control and $Smo^{L/L}$:$ChATCre^{+/-}$ mice (n = 1926-2357). *Right*: Average PC1 score per genotype. Unpaired t-test: ****p <0.0001.

(D) Same as (C), for control and $SmoM2^{C/-}$:$ChATCre^{+/-}$ mice (n =1827-2445). Unpaired t-test: ****p <0.0001.

(E) Parameters correlating with PC1 in datasets from control vs. $Smo^{L/L}$:$ChATCre^{+/-}$ (purple) and control vs. $SmoM2^{C/-}$:$ChATCre^{+/-}$ (gold). Parameters are grouped by feature type and ranked by factor loading. Rightmost column lists features with strong contributions to PC1 in both datasets (|factor loading| > 0.5).

Supplementary Figure 7. SmoM2 disrupts degree to which ACh predicts DA

Maximum correlation at positive lag, reflecting the extent to which changes in ACh predict future changes in DA (see also Fig. 3A). *Left*: Correlation coefficient; *Right*: timing of maximum correlation. *Top:* $Smo^{L/L}$:$ChATCre^{+/-}$ (n = 7-9). One-way ANOVA: ns. *Bottom:* $SmoM2^{C/-}$:$ChATCre^{+/-}$ (n = 8-10). Unpaired t-test: coefficient, *p <0.05. Mann-Whitney: timing, *p <0.05.

Supplementary Figure 8. Smo ablation from cholinergic neurons enhances sustained lever pressing in a progressive ratio task

(A) Cumulative lever press distribution during a progressive ratio 2 (PR2) session (n = 8-12). Two-way ANOVA: time elapsed, $F(2.089,37.60) = 205.10$, $p < 0.0001$; genotype, $F(1,18) = 5.22$, $p < 0.05$; interaction, $F(117,2106) = 3.45$, $p < 0.0001$. *Inset*: Total presses across the 2-hour session. Unpaired t-test: ns.

(B) Average latency to complete 50% of total presses. Unpaired t-test: *p < 0.05.

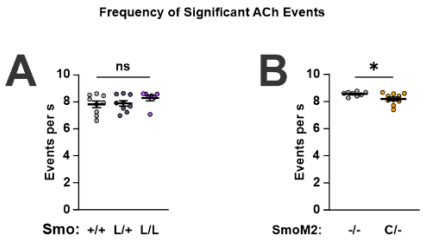

Supplementary Figure 1

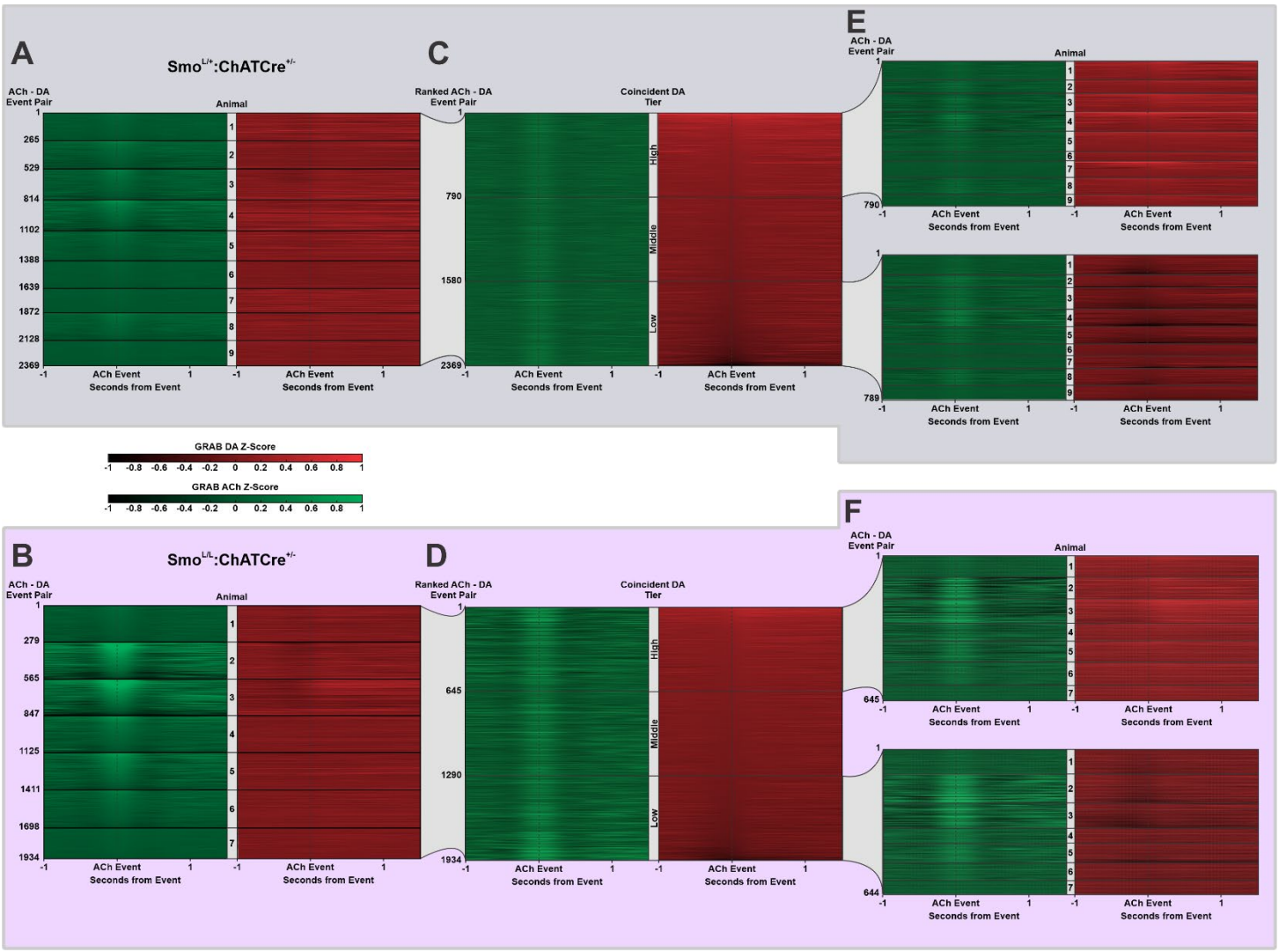

Supplementary Figure 2

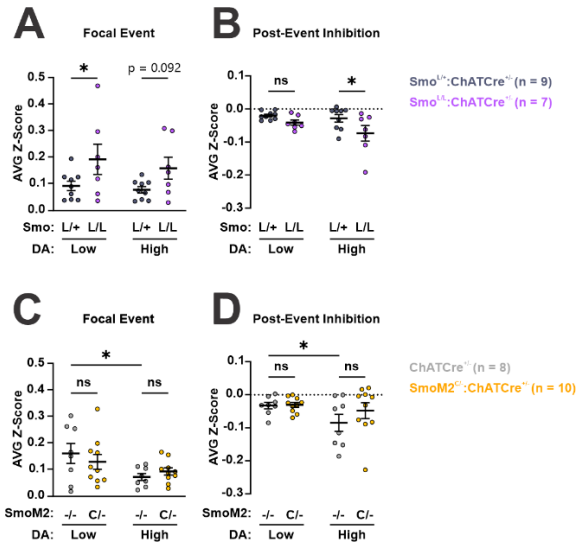

Supplementary Figure 3

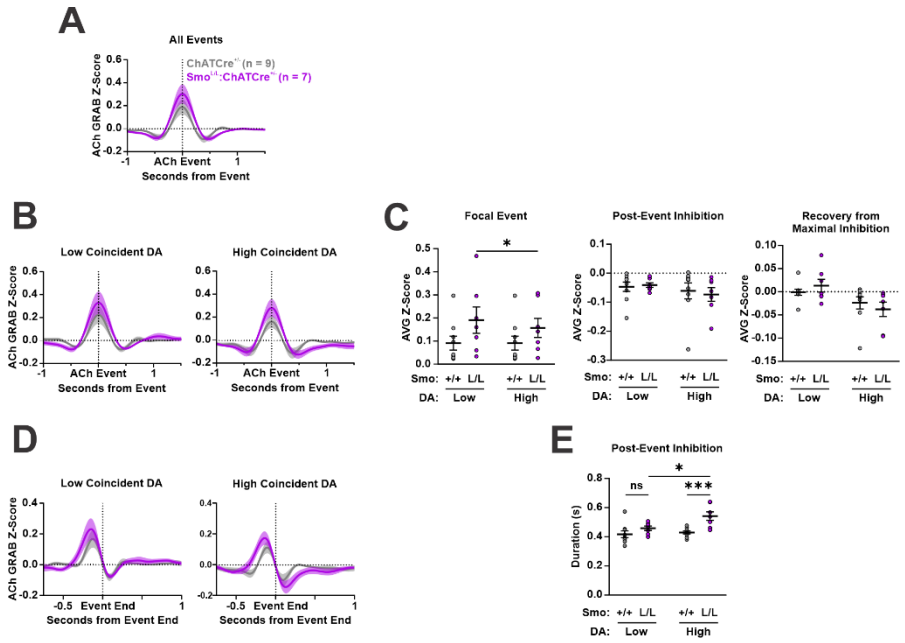

Supplementary Figure 4

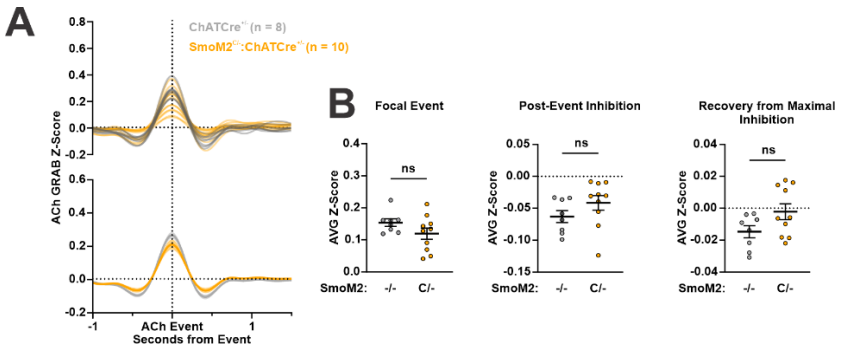

Supplementary Figure 5

A

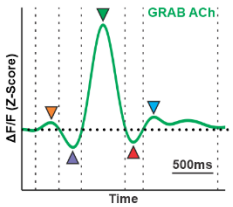

B

	Feature Size
1	Pre-Event Peak Magnitude
2	Pre-Event Dip Magnitude
3	Focal Event Magnitude
4	Post-Event Dip Magnitude
5	Post-Event Rebound Magnitude
6	Pre-Event Dip AUC
7	Focal Event AUC
8	Post-Event Dip AUC
9	Pre-Event Dip Average Fluorescence
10	Focal Event Average Fluorescence
11	Post-Event Dip Average Fluorescence
12	Focal Event Duration

	Average Rate of Change
13	1st Derivative Pre-Event Peak : Pre-Event Dip
14	1st Derivative Pre-Event Dip : Focal Event
15	1st Derivative Focal Event : Post-Event Dip
16	1st Derivative Post-Event Dip : Post-Event Rebound
17	2nd Derivative Pre-Event Peak : Pre-Event Dip
18	2nd Derivative Pre-Event Dip : Focal Event
19	2nd Derivative Focal Event : Post-Event Dip
20	2nd Derivative Post-Event Dip : Post-Event Rebound

	Relative Measures
21	Delta Pre-Event Peak : Pre-Event Dip
22	Delta Pre-Event Dip : Focal Event
23	Delta Focal Event : Post-Event Dip
24	Delta Post-Event Dip : Post-Event Rebound
25	AUC Pre-Event Peak : Focal Event
26	AUC Pre-Event Dip : Post-Event Dip
27	AUC Focal Event : Post-Event Rebound

	Feature Timing
28	Latency to Pre-Event Peak
29	Latency to Pre-Event Dip
30	Latency to Post-Event Dip
31	Latency to Post-Event Rebound

	Associated DA
32	DA Magnitude at time of Pre-Event Peak
33	DA Magnitude at time of Pre-Event Dip
34	DA Magnitude at time of Focal Event
35	DA Magnitude at time of Post-Event Dip
36	DA Magnitude at time of Post-Event Rebound
37	Average DA across Pre-Event Dip
38	Average DA across Focal Event
39	Average DA across Post-Event Dip
40	Delta DA Pre-Event Peak : Focal Event
41	Delta DA Pre-Event Dip : Post-Event Dip
42	Delta DA Focal Event : Post-Event Rebound

	ACh - DA Cross Correlation
43	Average Cross Correlation
44	Max Correlation with Positive Lag
45	Min Correlation with Positive Lag
46	Max Correlation with Negative Lag
47	Min Correlation with Negative Lag
48	Lag Value of Max Correlation with Positive Lag
49	Lag Value of Min Correlation with Positive Lag
50	Lag Value of Max Correlation with Negative Lag
51	Lag Value of Min Correlation with Negative Lag

C

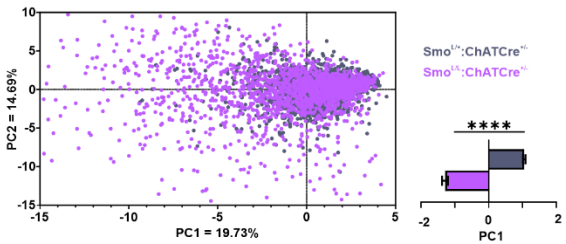

D

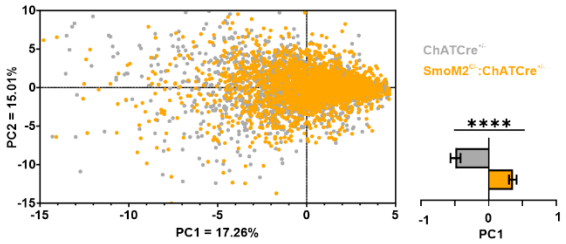

E

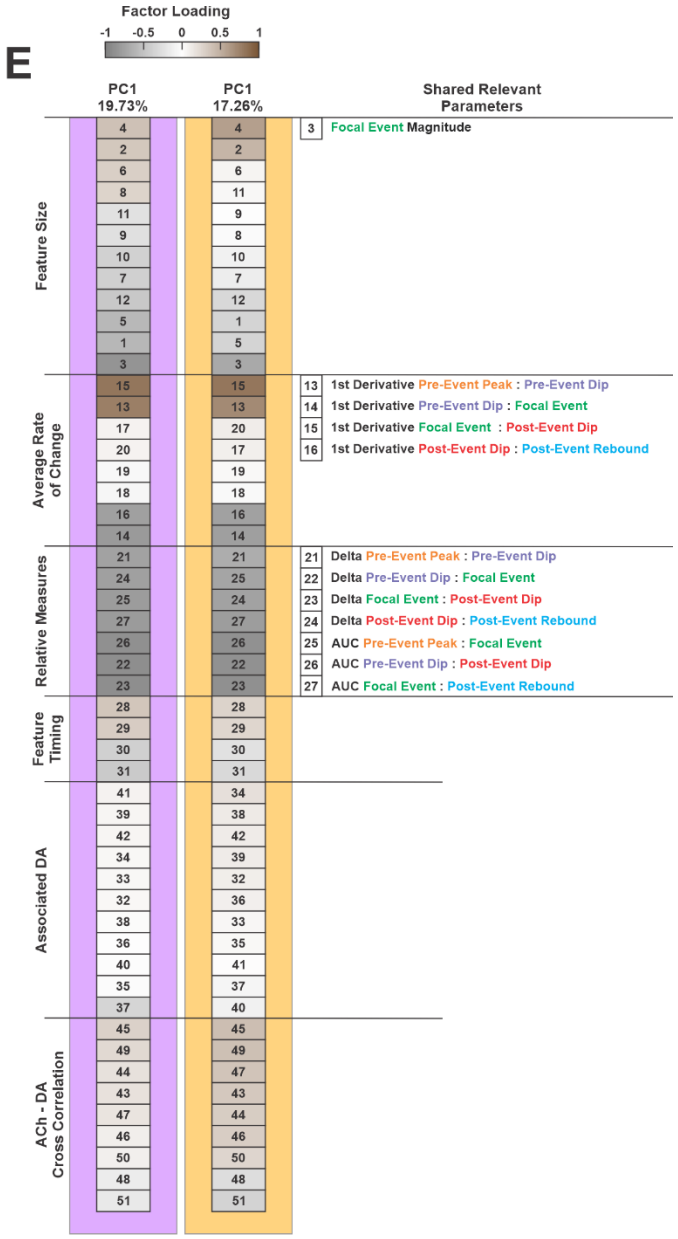

Supplementary Figure 6

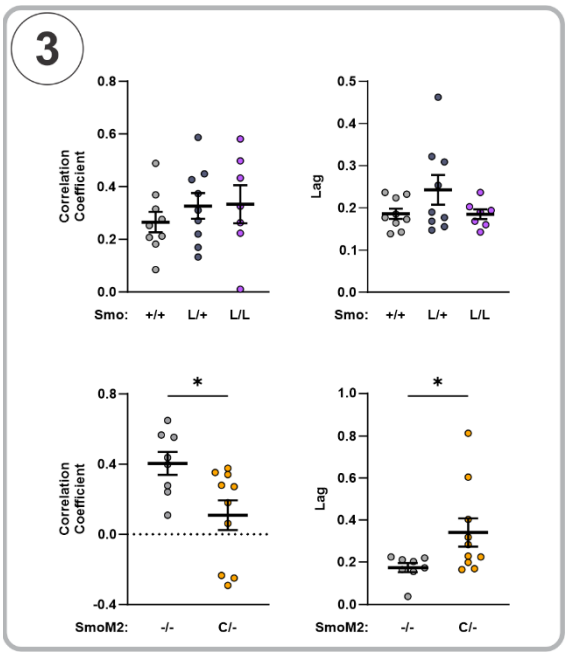

Supplementary Figure 7

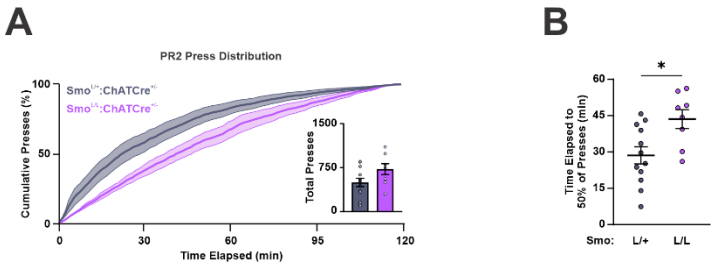

Supplementary Figure 8

References

Aoki, S., A. W. Liu, A. Zucca, S. Zucca and J. R. Wickens (2015). "Role of Striatal Cholinergic Interneurons in Set-Shifting in the Rat." J Neurosci **35**(25): 9424-9431.

Aosaki, T., A. M. Graybiel and M. Kimura (1994). "Effect of the nigrostriatal dopamine system on acquired neural responses in the striatum of behaving monkeys." Science **265**(5170): 412-415.

Aosaki, T., H. Tsubokawa, A. Ishida, K. Watanabe, A. M. Graybiel and M. Kimura (1994). "Responses of tonically active neurons in the primate's striatum undergo systematic changes during behavioral sensorimotor conditioning." J Neurosci **14**(6): 3969-3984.

Apicella, P., S. Ravel, M. Deffains and E. Legallet (2011). "The role of striatal tonically active neurons in reward prediction error signaling during instrumental task performance." J Neurosci **31**(4): 1507-1515.

Arensdorf, A. M., M. E. Dillard, J. M. Menke, M. W. Frank, C. O. Rock and S. K. Ogden (2017). "Sonic Hedgehog Activates Phospholipase A2 to Enhance Smoothened Ciliary Translocation." Cell Rep **19**(10): 2074-2087.

Bagnoli, E., Y. E. Lin, S. Burel, E. Jaimon, O. Antico, C. Themistokleous, J. M. Nikoloff, S. Squires, I. Morella, J. O. Watzlawik, F. C. Fiesel, W. Springer, F. Tonelli, P. Lis, S. P. Brooks, S. B. Dunnett, R. Brambilla, D. R. Alessi, S. R. Pfeffer and M. M. K. Muqit (2025). "Endogenous LRRK2 and PINK1 function in a convergent neuroprotective ciliogenesis pathway in the brain." Proc Natl Acad Sci U S A **122**(5): e2412029122.

Bastide, M. F., W. G. Meissner, B. Picconi, S. Fasano, P. O. Fernagut, M. Feyder, V. Francardo, C. Alcacer, Y. Ding, R. Brambilla, G. Fisone, A. Jon Stoessl, M. Bourdenx, M. Engeln, S. Navailles, P. De Deurwaerdere, W. K. Ko, N. Simola, M. Morelli, L. Groc, M. C. Rodriguez, E. V. Gurevich, M. Quik, M. Morari, M. Mellone, F. Gardoni, E. Tronci, D. Guehl, F. Tison, A. R. Crossman, U. J. Kang, K. Steece-Collier, S. Fox, M. Carta, M. Angela Cenci and E. Bezard (2015). "Pathophysiology of L-dopa-induced motor and non-motor complications in Parkinson's disease." Progress in neurobiology **132**: 96-168.

Bertran-Gonzalez, J., V. Laurent, B. C. Chieng, M. J. Christie and B. W. Balleine (2013). "Learning-related translocation of delta-opioid receptors on ventral striatal cholinergic interneurons mediates choice between goal-directed actions." J Neurosci **33**(41): 16060-16071.

Bijlsma, M. F., K. S. Borensztajn, H. Roelink, M. P. Peppelenbosch and C. A. Spek (2007). "Sonic hedgehog induces transcription-independent cytoskeletal rearrangement and migration regulated by arachidonate metabolites." Cellular signalling **19**(12): 2596-2604.

Bradfield, L. A., J. Bertran-Gonzalez, B. Chieng and B. W. Balleine (2013). "The thalamostriatal pathway and cholinergic control of goal-directed action: interlacing new with existing learning in the striatum." Neuron **79**(1): 153-166.

Chuhma, N., S. Mingote, H. Moore and S. Rayport (2014). "Dopamine neurons control striatal cholinergic neurons via regionally heterogeneous dopamine and glutamate signaling." Neuron **81**(4): 901-912.

Cooper, R. L., E. Jahanbakhsh, G. N. Santos Duran and M. C. Milinkovitch (2025). "Exacerbated sonic hedgehog signalling promotes a transition from chemical pre-patterning of chicken reticulate scales to mechanical skin folding." Open Biol **15**(4): 240342.

Delgado, I. and M. Torres (2016). "Gradients, waves and timers, an overview of limb patterning models." Semin Cell Dev Biol **49**: 109-115.

Duhne, M., A. Mohebi, K. Kim, L. Pelattini and J. D. Berke (2024). "A mismatch between striatal cholinergic pauses and dopaminergic reward prediction errors." Proc Natl Acad Sci U S A **121**(41): e2410828121.

Gallo, E. F., J. Greenwald, J. Yeisley, E. Teboul, K. M. Martyniuk, J. M. Villarin, Y. Li, J. A. Javitch, P. D. Balsam and C. Kellendonk (2022). "Dopamine D2 receptors modulate the cholinergic pause and inhibitory learning." Mol Psychiatry **27**(3): 1502-1514.

Girasole, A. E., M. Y. Lum, D. Nathaniel, C. J. Bair-Marshall, C. J. Guenthner, L. Luo, A. C. Kreitzer and A. B. Nelson (2018). "A Subpopulation of Striatal Neurons Mediates Levodopa-Induced Dyskinesia." Neuron **97**(4): 787-795 e786.

Gonzalez-Reyes, L. E., M. Verbitsky, J. Blesa, V. Jackson-Lewis, D. Paredes, K. Tillack, S. Phani, E. R. Kramer, S. Przedborski and A. H. Kottmann (2012). "Sonic hedgehog maintains cellular and neurochemical homeostasis in the adult nigrostriatal circuit." Neuron **75**(2): 306-319.
Graybiel, A. M., T. Aosaki, A. W. Flaherty and M. Kimura (1994). "The basal ganglia and adaptive motor control." Science **265**(5180): 1826-1831.
Harwell, C. C., P. R. Parker, S. M. Gee, A. Okada, S. K. McConnell, A. C. Kreitzer and A. R. Kriegstein (2012). "Sonic hedgehog expression in corticofugal projection neurons directs cortical microcircuit formation." Neuron **73**(6): 1116-1126.
Hobson, B. D., S. J. Choi, E. V. Mosharov, R. K. Soni, D. Sulzer and P. A. Sims (2022). "Subcellular proteomics of dopamine neurons in the mouse brain." Elife **11**.
Joshua, M., A. Adler, R. Mitelman, E. Vaadia and H. Bergman (2008). "Midbrain dopaminergic neurons and striatal cholinergic interneurons encode the difference between reward and aversive events at different epochs of probabilistic classical conditioning trials." J Neurosci **28**(45): 11673-11684.
Khan, S. S., E. Jaimon, Y. E. Lin, J. Nikoloff, F. Tonelli, D. R. Alessi and S. R. Pfeffer (2024). "Loss of primary cilia and dopaminergic neuroprotection in pathogenic LRRK2-driven and idiopathic Parkinson's disease." Proc Natl Acad Sci U S A **121**(32): e2402206121.
Khan, S. S., Y. Sobu, H. S. Dhekne, F. Tonelli, K. Berndsen, D. R. Alessi and S. R. Pfeffer (2021). "Pathogenic LRRK2 control of primary cilia and Hedgehog signaling in neurons and astrocytes of mouse brain." Elife **10**.
Kimura, M., J. Rajkowski and E. Evarts (1984). "Tonically discharging putamen neurons exhibit set-dependent responses." Proc Natl Acad Sci U S A **81**(15): 4998-5001.
Kosillo, P., Y. F. Zhang, S. Threlfell and S. J. Cragg (2016). "Cortical Control of Striatal Dopamine Transmission via Striatal Cholinergic Interneurons." Cereb Cortex **26**(11): 4160-4169.
Krok, A. C., M. Maltese, P. Mistry, X. Miao, Y. Li and N. X. Tritsch (2023). "Intrinsic dopamine and acetylcholine dynamics in the striatum of mice." Nature **621**(7979): 543-549.
Lim, S. A., U. J. Kang and D. S. McGehee (2014). "Striatal cholinergic interneuron regulation and circuit effects." Front Synaptic Neurosci **6**: 22.
Lin, Y. E., E. Jaimon, F. Tonelli and S. R. Pfeffer (2025). "Pathogenic LRRK2 mutations cause loss of primary cilia and Neurturin in striatal parvalbumin interneurons." Life Sci Alliance **8**(1).
Malave, L., D. R. Zuelke, S. Uribe-Cano, L. Starikov, H. Rebholz, E. Friedman, C. Qin, Q. Li, E. Bezard and A. H. Kottmann (2021). "Dopaminergic co-transmission with sonic hedgehog inhibits abnormal involuntary movements in models of Parkinson's disease and L-Dopa induced dyskinesia." Commun Biol **4**(1): 1071.
Martyniuk, K. M., A. Torres-Herraez, D. C. Lowes, M. Rubinstein, M. A. Labouesse and C. Kellendonk (2022). "Dopamine D2Rs coordinate cue-evoked changes in striatal acetylcholine levels." Elife **11**.
Matamales, M., J. Gotz and J. Bertran-Gonzalez (2016). "Quantitative Imaging of Cholinergic Interneurons Reveals a Distinctive Spatial Organization and a Functional Gradient across the Mouse Striatum." PloS one **11**(6): e0157682.
Matityahu, L., N. Gilin, G. A. Sarpong, Y. Atamna, L. Tiroshi, N. X. Tritsch, J. R. Wickens and J. A. Goldberg (2023). "Acetylcholine waves and dopamine release in the striatum." Nat Commun **14**(1): 6852.
Maurice, N., M. Liberge, F. Jaouen, S. Ztaou, M. Hanini, J. Camon, K. Deisseroth, M. Amalric, L. Kerkerian-Le Goff and C. Beurrier (2015). "Striatal Cholinergic Interneurons Control Motor Behavior and Basal Ganglia Function in Experimental Parkinsonism." Cell Rep **13**(4): 657-666.
Menshykau, D., P. Blanc, E. Unal, V. Sapin and D. Iber (2014). "An interplay of geometry and signaling enables robust lung branching morphogenesis." Development **141**(23): 4526-4536.
Morris, G., D. Arkadir, A. Nevet, E. Vaadia and H. Bergman (2004). "Coincident but distinct messages of midbrain dopamine and striatal tonically active neurons." Neuron **43**(1): 133-143.
Okada, K., K. Nishizawa, R. Fukabori, N. Kai, A. Shiota, M. Ueda, Y. Tsutsui, S. Sakata, N. Matsushita and K. Kobayashi (2014). "Enhanced flexibility of place discrimination learning by targeting striatal cholinergic interneurons." Nat Commun **5**: 3778.

Ortega-de San Luis, C., M. A. Sanchez-Garcia, J. L. Nieto-Gonzalez, P. Garcia-Junco-Clemente, A. Montero-Sanchez, R. Fernandez-Chacon and A. Pascual (2018). "Substantia nigra dopaminergic neurons and striatal interneurons are engaged in three parallel but interdependent postnatal neurotrophic circuits." Aging Cell **17**(5): e12821.
Petralia, R. S., C. M. Schwartz, Y. X. Wang, M. P. Mattson and P. J. Yao (2011). "Subcellular localization of Patched and Smoothened, the receptors for Sonic hedgehog signaling, in the hippocampal neuron." J Comp Neurol **519**(18): 3684-3699.
Petralia, R. S., Y. X. Wang, M. P. Mattson and P. J. Yao (2012). "Subcellular distribution of patched and smoothened in the cerebellar neurons." Cerebellum **11**(4): 972-981.
Pickering, J. and M. Towers (2016). "Inhibition of Shh signalling in the chick wing gives insights into digit patterning and evolution." Development **143**(19): 3514-3521.
Ratna, D. D. and T. C. Francis (2025). "Extrinsic and intrinsic control of striatal cholinergic interneuron activity." Front Mol Neurosci **18**: 1528419.
Ravel, S., E. Legallet and P. Apicella (1999). "Tonically active neurons in the monkey striatum do not preferentially respond to appetitive stimuli." Exp Brain Res **128**(4): 531-534.
Russo, M., G. Pellegrino, H. Faure, L. Tirou, A. Sharif and M. Ruat (2024). "Characterization of Sonic Hedgehog transcripts in the adult mouse brain: co-expression with neuronal and oligodendroglial markers." Brain Struct Funct.
Schmidt, S., M. D. Luecken, D. Trumbach, S. Hembach, K. M. Niedermeier, N. Wenck, K. Pflugler, C. Stautner, A. Bottcher, H. Lickert, C. Ramirez-Suastegui, R. Ahmad, M. J. Ziller, J. C. Fitzgerald, V. Ruf, W. D. J. van de Berg, A. J. Jonker, T. Gasser, B. Winner, J. Winkler, D. M. Vogt Weisenhorn, F. Giesert, F. J. Theis and W. Wurst (2022). "Primary cilia and SHH signaling impairments in human and mouse models of Parkinson's disease." Nat Commun **13**(1): 4819.
Schulz, J. M. and J. N. Reynolds (2013). "Pause and rebound: sensory control of cholinergic signaling in the striatum." Trends in neurosciences **36**(1): 41-50.
Straub, C., N. X. Tritsch, N. A. Hagan, C. Gu and B. L. Sabatini (2014). "Multiphasic modulation of cholinergic interneurons by nigrostriatal afferents." The Journal of neuroscience : the official journal of the Society for Neuroscience **34**(25): 8557-8569.
Su, Y., Y. Yuan, S. Feng, S. Ma and Y. Wang (2017). "High frequency stimulation induces sonic hedgehog release from hippocampal neurons." Sci Rep **7**: 43865.
Wu, J. Y., S. J. Cho, K. Descant, P. H. Li, A. Shapson-Coe, M. Januszewski, D. R. Berger, C. Meyer, C. Casingal, A. Huda, J. Liu, T. Ghashghaei, M. Brenman, M. Jiang, J. Scarborough, A. Pope, V. Jain, J. L. Stein, J. Guo, R. Yasuda, J. W. Lichtman and E. S. Anton (2024). "Mapping of neuronal and glial primary cilia contactome and connectome in the human cerebral cortex." Neuron **112**(1): 41-55 e43.
Zhang, Y. and P. A. Beachy (2023). "Cellular and molecular mechanisms of Hedgehog signalling." Nat Rev Mol Cell Biol **24**(9): 668-687.
Zhang, Y. F. and S. J. Cragg (2017). "Pauses in Striatal Cholinergic Interneurons: What is Revealed by Their Common Themes and Variations?" Front Syst Neurosci **11**: 80.
Zhang, Y. F., J. N. J. Reynolds and S. J. Cragg (2018). "Pauses in Cholinergic Interneuron Activity Are Driven by Excitatory Input and Delayed Rectification, with Dopamine Modulation." Neuron **98**(5): 918-925 e913.

Methods

EXPERIMENTAL MODEL AND STUDY PARTICIPANT DETAILS

All procedures involving animals were conducted in accordance with the National Institutes of Health guidelines and were approved by the Institutional Animal Care and Use Committees of the City University of New York. Experiments were conducted in adult mice between 2 and 8 months of age, weighing between 16 and 34 g. Both male and female mice were used in approximately equal proportions for all experiments. Mice were maintained on a 12 h light/dark cycle with ad libitum access to food and water. Behavioral experiments and recordings were conducted during the light phase with efforts made to balance time-of-day testing across conditions. Animals were group housed for all behavioral experiments. For fiber photometry experiments, animals were group housed prior to surgery and then single housed for the duration of recovery and recording periods.

Genetic Strategy

Because $Smo^{L/L}$ and $SmoM2^{C/-}$ alleles were backcrossed onto different genetic backgrounds, each genetic model was compared to controls of the same background strain across experiments. Mice with conditional ablation of Smo from $ChAT^{+}$ cells were generated by crossing $Smo^{L/+}$:$ChATCre^{+/-}$ mice with $Smo^{L/L}$ mice, following an initial pairing of $ChATCre^{+/-}$ with $Smo^{L/L}$ on a 129/Sv background. To account for potential off-target effects of introducing the floxed Smo allele and to facilitate the generation of mutant and control littermates, heterozygous $Smo^{L/+}$:$ChATCre^{+/-}$ mice were included as controls in several experiments, as noted in the text. In some cases, $ChATCre^{+/-}$ mice with two intact Smo alleles also served as alternate controls. Mice with conditional $ChAT^{+}$ expression of the constitutively active Smo variant, SmoM2, were generated by crossing $SmoM2^{C/-}$ mice with $ChATCre^{+/-}$ mice on a C57BL/6 background. All animals were toe-clipped at 7-14 days of age, and tissue was collected for DNA extraction and subsequent PCR genotyping of the relevant alleles. Forward and reverse primers are listed in the Key Resources Table.

METHOD DETAILS

Pharmacology

Smoothened agonist (SAG hydrochloride) was purchased from Biosynth International Inc. and diluted in sterile water to a stock concentration of 10 mg/ml. The solution was aliquoted to avoid repeated freeze-thaw cycles and stored at -20 °C. For experiments, the stock was further diluted in saline so that a bolus of 10 µl per gram of body weight delivered a dose of 20 Mg/Kg.

Viral Constructs

The AAV5-Syn-ChrimsonR-tdT construct was obtained from Addgene for optogenetic stimulation experiments. For fluorescence-based detection of Acetylcholine and Dopamine, the following viral constructs were obtained from WZ Biosciences: green-fluorescent AAV9-hSyn-Ach3.0 and AAV9-hSynrDA2h (DA4.3h), and red-fluorescent AAV9-hSynrDA1h (rDA2.5h).

Implant Preparation

Nine-millimeter lengths of 400 µm-diameter optical fiber (FT400UMT; Thorlabs) were scored using a ruby fiber optic scribe (S90R; Thorlabs) and manually pulled to produce clean breaks. Fiber segments were then glued into 6.4mm-long ceramic ferrules (CFLC440; Thorlabs) with two-part epoxy and left to cure overnight. Implants were polished using a series of lapping sheets with decreasing grit sizes until light transduction efficiency reached ≥75%, as tested with a laser.

Surgical Procedures

Anesthesia for viral injections and fiber implantations was induced using a gas mixture of oxygen (1.5 L/min) and 4% isoflurane (Covetrus). Mice were positioned in a stereotaxic frame (Model 900; David Kopf Instruments) and maintained under anesthesia with 2-3% isoflurane throughout the surgery. A local anesthetic (70 µl bupivacaine) was administered subcutaneously under the scalp prior to incision. At the conclusion of surgery, 0.05 Mg/Kg buprenorphine (Buprenex) was administered subcutaneously, and mice were placed in clean home cages on a heating pad for recovery.

For optogenetic stimulation experiments, 0.5 µl of AAV carrying ChrimsonR-Tdt was injected into the substantia nigra pars compacta at coordinates AP: -3.2 mm, ML: +1.5 mm, DV: -4.1 mm. A second viral injection of 0.5 µl AAV encoding either the green-fluorescent GRAB DA or GRAB ACh sensor was delivered into the dorsolateral striatum at coordinates AP: +0.6 mm, ML: +2.2 mm, DV: -3.0 mm.

For dual-channel GRAB fluorescence recording experiments, a single 1 µl injection containing a 50:50 mixture of red-fluorescent GRAB DA and green-fluorescent GRAB ACh sensors was infused into the dorsolateral striatum at coordinates AP: +0.6 mm, ML: +2.2 mm, DV: -3.0 mm.

In both optogenetic stimulation and dual-channel GRAB fluorescence experiments, fiber implants were placed at coordinates AP: +0.6 mm, ML: +2.2 mm, DV: -3.0 mm, and secured using Metabond® (Parkell, Inc). In dual-channel GRAB fluorescence animals, a small burr hole was also made at lambda, and a custom headbar was affixed with a screw and secured with Metabond® to facilitate head fixation during recording sessions.

On the day following surgery, implant stability was confirmed, topical antibiotic was applied to the surgical site, and a dust cap (CAPL; Thorlabs) was affixed to protect the implant. A minimum of 2.5 weeks was allowed following surgery to ensure full recovery and sufficient viral expression before beginning experiments.

Optogenetic Experiments

Experiments were conducted in a 43 x 43 cm open-field arena (ENV-515S; Med Associates), isolated from ambient noise and light, and located in a room housing other mouse cages. Animal movements were recorded and analyzed using Noldus EthoVision XT video tracking system. Fluorescence measurements of DA or ACh levels were acquired using a Doric Lenses 5 port Fluorescence Mini Cube (ilFMC5-G3_IE(400-410)_E(460-490)_F(500-540)_O(580-680)_S). The Mini Cube was connected to a Laser Diode Fiber Light Source (LDFLS 465 nm/80 mW; Doric Lenses) via the

optogenetics (O) port using an optical patch cord (MFP_200/220/LWMJ-0.22_1m_FC-FCA; Doric Lenses). ChrimsonR excitation, GRAB sensor excitation, isosbestic excitation (405 nm), and signal collection were all performed through a single patch cord (MFP_200/220/LWMJ-0.37_1m_FCM-MF1.25(F)_LAF; Doric Lenses), connected to the animal's implanted optical fiber via an interconnect (ADAL3; Thorlabs), and to the sample (S) port of the Mini Cube. To reduce torsion and facilitate natural movement, the patch cord was supported by an aluminum wire suspended above the arena.

The Mini Cube, laser diode, signal acquisition, and synchronization with behavioral recordings (via a Noldus USB-IO box) were all controlled and modulated using a National Instruments USB-6343 multifunction I/O device. Signal timing and routing were programmed in WaveSurfer (Janelia), a MATLAB-based data acquisition platform. ChrimsonR stimulations consisted of 780 ms pulse trains delivered every 35 seconds using 590 nm light at 15Hz. Laser power was calibrated to deliver 15 mW/mm^2 at the tip of the implant. GRAB sensor excitation was performed using 10 ms pulses of 460 nm light at a frequency of 100 Hz, interleaved with isosbestic excitation using 10 ms pulses of 400 nm light at a frequency of 100 Hz. Emitted fluorescence was detected using the Mini Cube's silicon photodiode sensor (gain set to 10x) and digitized by WaveSurfer at a sampling rate of 1000 Hz.

At the start of each session, the animal's fiber implant was securely connected to the patch cord, and the animal was then placed in the center of the arena. Prior to the first stimulation session, animals were habituated in the arena for 20-60 minutes with the patch cord attached, but without ChrimsonR stimulation or GRAB sensor recording. On each of the seven stimulation days, animals were first habituated in the arena for 5 minutes before stimulation began. GRAB sensor recording was omitted on days 5 and 6 to preserve signal strength for the final stimulation day. Animals expressing the GRAB DA sensor underwent an eighth stimulation day, during which a challenge dose of SAG was administered to assess its effects on DA release (Fig. 1C-D). For all SAG-treated animals, intraperitoneal injections were administered 25 minutes prior to placement in the arena, during which animals remained in their home

cage. Data were collected from 5 independent cohorts: 2 for GRAB DA experiments and 3 for GRAB ACh experiments.

Data Processing

Data files (hierarchical data format version 5, HDF5) generated by WaveSurfer were analyzed using custom MATLAB scripts. Interleaved fluorescence and isosbestic signals from each optogenetic stimulation sweep were separated based on their respective excitation wavelength onset parameters. Peripheral samples from each signal onset were trimmed to account for excitation onset and sweep transition artifacts, and the resulting traces were concatenated into two continuous raw time series. True timestamps were retained to allow precise alignment with the onset of ChrimsonR stimulation. Fluorescence and isosbestic signals were then processed with a zero-phase low-pass filter at 20 Hz, followed by downsampling via a moving mean of 200 samples. ΔF/F% was calculated by fitting the isosbestic signal to the fluorescence signal using linear regression, subtracting the fit from the fluorescence signal, and dividing by the fit, then multiplying by 100. The timing of ChrimsonR stimulation (590 nm light) onset was used to extract 4.5-second ROIs from the ΔF/F% signal, anchored 1.5 seconds before the sample most closely aligned with each stimulation onset. Each individual ROI was then z-scored and baseline-normalized by subtracting the average fluorescence across a 0.5-second window preceding ChrimsonR stimulation from the entire ROI. All ROIs were then averaged to produce a session-averaged trace which was smoothed by applying a 100-sample moving mean.

Feature quantification

Area under the curve (AUC) for GRAB DA signals aligned to ChrimsonR stimulation was calculated for each session-averaged trace. The maximum fluorescence within a 1.5-second window following ChrimsonR stimulation onset was identified as the peak. Flanking inversion points- determined by changes in the sign of the first derivative of the signal and representing the points of maximal

difference from the peak- were identified as the start and end of the peak window. The AUC was then calculated using MATLAB's trapz function.

Dip and rebound durations for GRAB ACh signals aligned to ChrimsonR stimulation were similarly quantified for each session-averaged trace. Dips were identified as the first stretch of negative values following stimulation onset, beginning when the signal first crossed below zero and ending when it returned to zero or the trace ended, whichever came first. Rebounds were defined as the subsequent stretch of positive values, starting immediately after the dip ended and continuing until the signal returned to zero or the end of the trace. For both dips and rebounds, duration and timing of the minimum (for dips) or maximum (for rebounds) signal value were extracted.

Dual-Channel GRAB fluorescence Experiments

Experiments were conducted in a dark, sound attenuating cubicle (ENV-022MD; Med Associates) isolated from ambient noise and light. Fluorescence measurements of red GRAB DA and green GRAB ACh signals were acquired using a Doric Lenses 5 port Fluorescence Mini Cube (iFMC6_IE(400-410)_E1(460-490)_F1(500-540)_E2(555-570)_F2(580-680)_S), paired with a 4 channel LED driver (LEDD, Doric Lenses) and operated via Doric Neuroscience Studio software. Excitation of red and green GRAB sensors, isosbestic (405 nm) excitation, and fluorescence signal collection were all performed through a single patch cord (MFP_400/440/LWMJ-0.37_1m_FCM-MF1.25(F)_LAF; Doric Lenses), which was connected to the implanted optical fiber via a ceramic sleeve (ADAL1; Thorlabs) wrapped in foil. The other end of the patch cord was attached to the sample (S) port of the Mini Cube. The LED driver and signal acquisition were controlled and modulated using a National Instruments USB-6343 multifunction I/O device.

Red GRAB DA sensor excitation using 10 ms pulses of 555 nm light at a frequency of 33 Hz, green GRAB ACh sensor excitation using 10 ms pulses of 460 nm light at a frequency of 33 Hz, and isosbestic excitation using 10 ms pulses of 400 nm light at a frequency of 33 Hz were interleaved.

Emitted red and green fluorescence signals were detected using a pair of silicon photodiode Doric Fluorescence Detectors (DFD_FOA_FC), equipped with a spectral bandpass filter: 525/40 nm for green fluorescence and 630/92 nm for red fluorescence. Each detector was operated in DC detection mode with a gain of 10x, and signals were digitized using WaveSurfer at a sampling rate of 1000 Hz.

At the start of each session, the animal was head-fixed atop a running wheel inside the cubicle and the animal's fiber implant was connected to the patch cord. Prior to the first recording session, mice were habituated on three separate days for 15 minutes each to head fixation and movement on the running wheel, without GRAB sensor recording. On the day of recording, animals were placed in the apparatus and allowed to habituate for 10 minutes before 30 minutes of data collection. Data were collected from 8 independent cohorts: 5 for $Smo^{L/L}$:$ChATCre^{+/-}$ experiments and 3 for $SmoM2^{C/-}$:$ChATCre^{+/-}$ experiments.

Data Processing

Data files (hierarchical data format version 5, HDF5) generated by WaveSurfer were analyzed using custom MATLAB scripts. Interleaved red fluorescence, green fluorescence, and isosbestic signals were separated based on their respective excitation wavelength onset parameters. Peripheral samples from each signal onset were trimmed to account for excitation onset transients and potential crosstalk between channels. The resulting traces were concatenated into three continuous raw time series and aligned. Fluorescence and isosbestic signals were processed with a zero-phase low-pass filter at 20 Hz, followed by downsampling using a moving mean over 100 samples. $\Delta F/F\%$ was calculated for both red and green fluorescence signals by fitting the isosbestic signal to each fluorescence signal via linear regression, subtracting the fit from the fluorescence signal, dividing by the fit, and multiplying by 100. The full green and red $\Delta F/F\%$ traces were then z-scored.

To identify significant ACh Events, we applied a two-pass median absolute deviation (MAD) thresholding approach. First, a 30-second moving median and corresponding 30-second moving MAD

were computed across the full GRAB ACh z-scored trace. Samples exceeding the median plus 2 MADs were clipped, producing a filtered trace. A second 30-second moving median and MAD were then calculated from this filtered trace. ACh Events were recognized as discrete segments in the original z-scored trace that exceeded the filtered median plus 3 MADs. The maximal point of each segment was identified as the Focal Event of the ACh Event and used for event alignment.

For each event, a 6-second ROI was extracted. To prevent overlap between ROIs, subsequent events that overlapped with a preceding ROI were excluded. Corresponding 6-second ROIs from the aligned GRAB DA z-scored trace were also extracted. Each ROI was baseline-normalized by subtracting the average fluorescence during the first second of the ROI from the entire segment. All ROIs were then averaged to produce session-averaged traces.

Feature quantification

Each ACh Event was decomposed into a standardized set of features organized relative to the Focal Event (see Supplementary Fig. 6A). Inflection points flanking the Focal Event were identified by detecting sign changes in the first derivative of the trace. ACh Event features were defined as follows:

- Focal Event – the peak of the ACh Event, centered on the defining inflection point.
- Pre-Event Dip – the first inflection point preceding the Focal Event such that the absolute difference in magnitude between this dip and the next most distal inflection point is > 10% of the absolute difference in magnitude between this dip and the Focal Event.
- Pre-Event Peak – the inflection point immediately preceding the Pre-Event Dip.
- Post-Event Dip - the first inflection point following the Focal Event such that the absolute difference in magnitude between this dip and the next most distal inflection point is > 10% of the absolute difference in magnitude between this dip and the Focal Event.
- Post-Event Rebound - the inflection point immediately following the Post-Event Dip, or the end of the trace, whichever occurs first.

Feature boundaries were defined as the first baseline crossings (i.e., points where the signal returns to zero) flanking each identifying inflection. Recovery from Maximal Inhibition was defined as the segment beginning at the inflection point identified as the Post-Event Dip and extending to the end of the trace. For each feature, the following measures were extracted: magnitude, timing relative to Focal Event, duration, delta (i.e., change in magnitude relative to the Focal Event), AUC relative to baseline, AUC relative to the position of flanking features, first derivate, second derivative, and average fluorescence.

Trace Stratification and Realignment

Stratification of ACh Events based on coincident DA was performed by grouping all ACh Events from a given condition, then ranking them by the magnitude of their coincident DA signal at the time of ACh Event peak. The ranked traces were split into thirds (high, middle, low tiers), and traces within each tier were averaged based on the animal they originated from. For realignment (Fig. 2I) individual ACh Events within each tier of DA-stratified events were aligned to the start of the Post-Event Dip (defined as the final baseline point prior to the inflection point identified as the Post-Event Dip). Animal-level averages were then produced for each tier.

Behavioral Experiments

Rotarod

Trials were conducted in a room with low ambient light and noise using a five-lane mouse rotarod (ENV-574M; Med Associates) programmed to accelerate linearly from 4 to 40 RPM over 300 seconds (preset speed setting #9). After reaching top speed, the trial continued for an additional 400 seconds to assess sustained physical performance and motor skill retention. Mice underwent 10 trials per day for 8 consecutive days. Latency to fall was recorded for each trial. A fall was defined as either falling off the rod or clinging and completing a full passive rotation around the rod. In the latter case, the mouse was manually removed and placed in the bottom of the apparatus. Mice that remained on the rod for the full

700 were also manually removed and placed in the bottom. Mice were allowed approximately 3-5 minutes of rest between trials. As described in the text, the learning criterion was defined as the first day on which a mouse completed the acceleration phase (>300 seconds latency to fall) in more than trials. Data were recorded by an experimenter blinded to genotype and collected from 8 independent cohorts: 5 for $Smo^{L/L}$:$ChATCre^{+/-}$ experiments and 3 for $SmoM2^{C/-}$:$ChATCre^{+/-}$ experiments.

Lever Pressing

Operant training was performed in a Med Associates modular chamber (ENV-008) with a steel grid floor (ENV-307A-GFW; Med Associates), located in a room housing other mouse cages but isolated from ambient noise. A reward magazine (ENV-303M-4.25; Med Associates) equipped with a head entry detector (ENV-303HDA; Med Associates) was positioned at mouse eye-level in the center of one wall, with a retractable lever (ENV-312-3M; Med Associates) located to the left of the magazine. Chocolate-flavored sucrose pellets (F05301; Bio-Serv) were used as rewards and delivered via an automated pellet dispenser (ENV-203; Med Associates). All equipment was controlled via a Noldus USB-IO box programmed using the Noldus EthoVision XT behavior tracking system.

Animals were first food-restricted to 85% of their baseline body weight and maintained at this weight throughout the experiment by allowing ad libitum access to chow for one hour following each daily lever pressing session. Each session began with a 5-minute habituation period, after which the lever extended and remained available for the full 1-hour session. Head entries, lever presses, and reward deliveries were recorded during all sessions.

Training began with a continuous reinforcement (CRF) phase, during which the magazine and lever were baited with pellet crumbs at the start of the session, and every lever press resulted in a reward. To advance from CRF training, animals were required to complete a minimum of three training days and reach a criterion of 50 presses within a single session—the maximum number of rewards available during

this phase. Animals that did not reach this threshold within the first three days continued CRF training until the criterion was met before progressing to the next reinforcement schedule.

Following CRF training, animals underwent Random Interval 15 (RI15) training, in which an average interval of 15 seconds (range: 0-30 s) had to elapse before lever presses elicited subsequent rewards. After three days of RI15, animals underwent a 15-minute devaluation probe. Prior to the session they were given ad libitum access to either chocolate-flavored sucrose pellets (devalued condition) or standard lab chow (baseline condition). Animals were then placed in the chamber, and lever presses were recorded in the absence of reward delivery.

Animals subsequently completed 8 days of Random Interval 30 (RI30) training, in which an average of 30 seconds (range: 0-60 s) had to elapse before a lever press was rewarded. For Progressive Ratio 2 (PR2) testing, animals were first required to complete 3 days of CRF, 3 days of RI15, and 6 days of RI30 training, as described above. In the PR2 paradigm, the first reward was delivered after a single press, and the number of presses required for each subsequent reward doubled. PR2 sessions lasted 2 hours and were prematurely terminated if 2 consecutive minutes elapsed without any lever presses. Data for all experiments were pooled from 2 independent cohorts.

QUANTIFICATION AND STATISTICAL ANALYSIS

All statistical analyses were performed using GraphPad Prism version 10.0.0 for Windows (GraphPad Software, Boston, Massachusetts USA; www.graphpad.com). Statistical tests used, group sizes, p values, and other relevant details are reported in the figure legends. The marker “ns” indicates results that were not significant. Mann-Whitney nonparametric tests were used when F-tests for equality of variances indicated unequal variance between groups. All figures display group averages ±SEM. Fiber photometry data processing, analysis, and feature quantification were performed using MATLAB version 9.12.0 (R2022a) for Windows (The MathWorks Inc., Natick, Massachusetts USA; www.mathworks.com).

Key resources table

REAGENT or RESOURCE	SOURCE	IDENTIFIER
Antibodies		
Bacterial and virus strains		
AAV5-Syn-ChrimsonR-tdT	Addgene	Plasmid #59171
AAV9-hSyn-Ach3.0	WZ Biosciences	N/A
AAV9-hSynrDA2h (DA4.3h)	WZ Biosciences	N/A
AAV9-hSynrDA1h (rDA2.5h)	WZ Biosciences	N/A
Biological samples		
Chemicals, peptides, and recombinant proteins		
SAG hydrochloride	Biosynth International Inc.	FS76762
Critical commercial assays		
Deposited data		
Experimental models: Cell lines		
Experimental models: Organisms/strains		

Mouse: B6;129S6-*Chat*$^{tm2(cre)Lowl}$/J	The Jackson Laboratory	IMSR_JAX:006410
Mouse: *Smo*^{tm2Amc}/J	The Jackson Laboratory	IMSR_JAX:004526
Mouse: *Gt(ROSA)26Sor*$^{tm1(Smo/EYFP)Amc}$/J	The Jackson Laboratory	IMSR_JAX:005130
Oligonucleotides		
Primer: ChATCre Common Reverse: CAG GGT TAG TAG GGG GTC AC	The Jackson Laboratory	23357
Primer: ChATCre Mutant Forward: CAA AAG CGC TCT GAA GTT CCT	The Jackson Laboratory	23358
Primer: ChATCre Wildtype Forward: GCA AAG AGA CCT CAT CTG TGG A	The Jackson Laboratory	23359
Primer: Smo$^{L/L}$ Common Forward: GGA CTC GCA GGA GGA AGC	The Jackson Laboratory	24153
Primer: Smo$^{L/L}$ Wildtype Reverse: CAA CAG TTT GAG GCC TGA GC	The Jackson Laboratory	24155
Primer: Smo$^{L/L}$ Mutant Reverse: CTC CAG ACT GCC TTG GGA AAA	The Jackson Laboratory	oIMR8619
Primer: SmoM2 Mutant Forward: CTG ACC CTG AAG TTC ATC TGC	This Paper	N/A
Primer: SmoM2 Mutant Reverse: GTG CGC TCC TGG ACG TAG	This Paper	N/A
Primer: Rosa26 Wildtype Forward: CTC TTC CCT CGT GAT CTG CAA CTC C	This Paper	N/A
Primer: Rosa26 Wildtype Reverse: CAT GTC TTT AAT CTA CCT CGA TGG	This Paper	N/A
Recombinant DNA		
Software and algorithms		
EthoVision XT	Noldus	Version 10.0.828
WaveSurfer	Janelia	Version 1.0.6
MATLAB R2022a	The MathWorks Inc.	Version 9.12.0
Doric Neuroscience Studio	Doric	Version 5.4.1.1
Other		
20 mg Chocolate-flavored Sucrose Pellets	Bio-Serv	F05301